Sampling Errors in Wind Fields Constructed from Single and Tandem Scatterometer Datasets

MICHAEL G. SCHLAX, DUDLEY B. CHELTON, AND MICHAEL H. FREILICH

College of Oceanic and Atmospheric Sciences, Oregon State University, Corvallis, Oregon

ABSTRACT

Sampling patterns and sampling errors from various scatterometer datasets are examined. Four single and two tandem scatterometer mission scenarios are considered. The single scatterometer missions are ERS (with a single, narrow swath), NSCAT and ASCAT (dual swaths), and QuikSCAT (a single, broad swath obtained from the SeaWinds instrument). The two tandem scenarios are combinations of the broad-swath SeaWinds scatterometer with ASCAT and QuikSCAT. The dense, nearly uniform distribution of measurements within swaths, combined with the relatively sparse, nonuniform placement of the swaths themselves create complicated space–time sampling patterns. The temporal sampling of all of the missions is characterized by bursts of closely spaced samples separated by longer gaps and is highly variable in both latitude and longitude. Sampling errors are quantified by the expected squared bias of particular linear estimates of component winds. Modifications to a previous method that allow more efficient expected squared bias calculations are presented and applied. Sampling errors depend strongly on both the details of the temporal sampling of each mission and the assumed temporal scales of variability in the wind field but are relatively insensitive to different spatial scales of variability. With the exception of ERS, all of the scatterometer scenarios can be used to make low-resolution (3° and 12 days) wind component maps with errors at or below the 1 m s^{-1} level. Only datasets from the broad-swath and tandem mission scenarios can be used for higher-resolution maps with similar levels of error, emphasizing the importance of the improved spatial and temporal coverage of those missions. A brief discussion of measurement errors concludes that sampling error is generally the dominant term in the overall error budget for maps constructed from scatterometer datasets.

1. Introduction

Scatterometers obtain measurements of wind velocity from the normalized radar cross-section of the ocean (Naderi et al. 1991) in swaths that parallel the ground track of the spacecraft. Figure 1 shows typical data distributions over part of the North Pacific Ocean for a single pass of each of four past, present, and proposed scatterometers. The common characteristic of these instruments is the dense, almost uniform spacing of data within each measurement swath. As discussed in detail in section 2, the measurement swaths themselves form a relatively sparse and complex space–time pattern. This combination of dense, within-swath sampling, and the irregular sampling of the swaths themselves complicates analysis of the sampling characteristics of scatterometer data. Within each swath, standard notions of sampling theory (e.g., the concept of Nyquist sampling) can be useful, but for the dataset as a whole, more general methods are required.

Scatterometer wind measurements are often used to construct wind component maps on a uniform space–time grid. For example, the mapped winds may be used to calculate wind divergence or vorticity, or as an input to a numerical meteorological or oceanographic model. Interpolation or smoothing algorithms are necessary to generate wind component maps on a regular grid from the irregular measurements. A variety of these algorithms are available and have been used for scatterometer data, including various forms of objective analysis (e.g., Kelly and Caruso 1990), the successive correction method (Liu et al. 1998), and simple bin and weighted averaging schemes (Legler and O'Brien 1985; Zeng and Levy 1995). All of these methods act as low-pass filters so that larger space scales and timescales are preferentially retained in the estimates. When applied to unevenly distributed measurements, any interpolation algorithm will also retain shorter scales of variability that are not resolved by the data. This manifestation of aliasing in its most general form results in ''sampling errors'' in the mapped fields that are distinct from the consequences of measurement errors.

The presence of significant sampling errors in scatterometer datasets is well known. Legler and O'Brien (1985) carried out a simulation similar to that described

Corresponding author address: Michael G. Schlax, College of Oceanic and Atmospheric Sciences, Oregon State University, 104 Ocean Admin Building, Corvallis, OR 97331-5503.
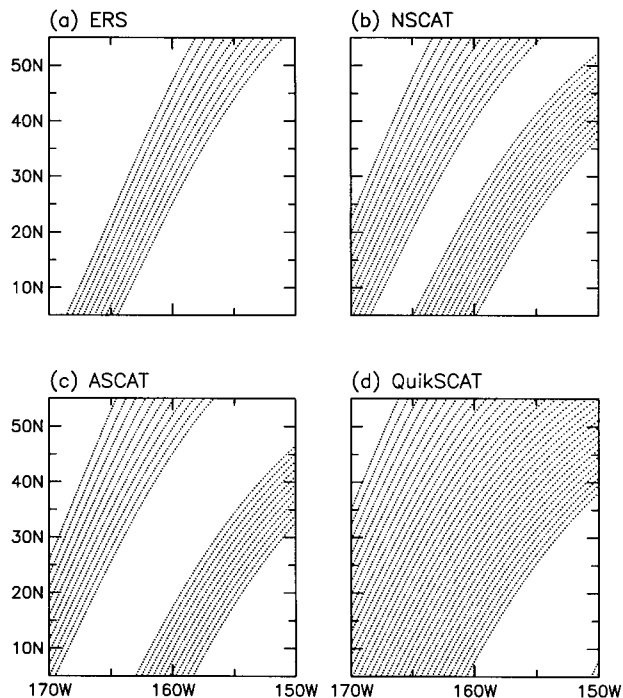E-mail: schlax@pepper.oce.orst.edu

FIG. 1. Measurement locations for a single pass over the North Pacific Ocean for each of the single-scatterometer missions. (a) ERS, (b) NSCAT, (c) ASCAT, and (d) QuikSCAT.

below. They concluded that the primary limitation for maps constructed from the NSCAT-like scatterometer dataset that they considered was sampling, rather than measurement error. Kelly and Caruso (1990) developed an objective method for interpolating NSCAT scatterometer data and performed simulations [using European Center for Medium-Range Weather Forecasts (ECMWF) analyses] and an extensive analysis of the errors of the gridded fields they produced. Zeng and Levy (1995) studied aliasing in monthly mean wind fields from the European Remote Sensing Satellite (ERS) scatterometer and devised an interpolation scheme to mitigate the patterns resulting from sampling errors that appear in monthly mean wind maps derived from ERS data.

A simple simulation demonstrates the nature of the scatterometer wind velocity sampling errors that can be expected. Analyzed surface wind fields from the ECMWF were obtained on a $1° \times 1°$, 6-h grid and subsampled using trilinear interpolation at the NSCAT measurement locations. Both the gridded and subsampled model winds were interpolated onto a $1° \times 1°$, daily space–time grid. The zonal and meridional components were individually interpolated using a quadratic loess smoother (Cleveland 1979, Cleveland and Devlin 1988; see also Schlax and Chelton 1992, and Greenslade et al. 1997). Figures 2 and 3 compare the maps that resulted from interpolating the full and subsampled model fields at two specific times, for two different lev-

els of applied smoothing (the times are from an arbitrary reference and do not represent actual dates).

Figure 2 shows maps made to retain scales larger than approximately 200 km and 4 days. The top row shows the maps at day 45 made by interpolating the full analyses (left) and the NSCAT subsampled analyses (center). The differences between these two maps (right) result from the NSCAT subsampling and are thus sampling errors. The bottom row contains similar maps for day 55. The difference maps show mean sampling errors of 2.1 m s^{-1}, with a maximum error of 10.4 m s^{-1}. Note that the largest errors (around 28°N, 168°W on day 55) are not associated with the strongest winds (which occur on day 45).

The maps in Fig. 3 retain scales larger than approximately 600 km zonally, 200 km meridionally, and 10 days. The sampling errors for these larger scales have changed, and now average 1.2 m s^{-1} with a maximum error of 4.2 m s^{-1}. The 3–4 m s^{-1} errors on day 45 in Fig. 2c at 32°N, 168°W have expanded in Fig. 3c to cover the range 30°–40°N. The errors forming the semi-circular band in the center of Fig. 2c have been reduced in magnitude as have the largest errors noted on day 55. The general reduction of the mean and variability of the sampling errors in the smoother maps is an indication that the NSCAT sampling is better able to resolve the larger space and longer timescales present in the ECMWF field. The sampling errors alone from NSCAT can amount to a significant percentage of the true wind field and are spatially and temporally inhomogeneous. Moreover, the errors change when the amount of smoothing applied to the data changes, and do not necessarily decrease locally with increased smoothing. Clearly a quantification of the magnitude and spatial–temporal distribution of sampling error is essential.

The effects of sampling errors on maps of component wind fields are conveniently expressed in terms of the expected squared bias (ESB). Suppose that $\bar{h}$ represents the value that a given interpolation algorithm would return when applied to a continuously sampled, error-free dataset. Let $\hat{h}$ be the estimate given by the interpolation algorithm when applied to an actual dataset, assumed to be nonuniformly sampled and contaminated by measurement error. Because of sampling and measurement error, $\hat{h}$ will differ from $\bar{h}$. The error of $\hat{h}$ as an estimator of $\bar{h}$ can be characterized by the mean-squared error mse $= E[(\bar{h} - \hat{h})^2]$, where E denotes the expected value over realizations of the dataset. The mse can also be written in the form

$$\text{mse} = E[(\bar{h} - E[\hat{h}])^2] + E[(\hat{h} - E[\hat{h}])^2], \quad (1)$$

in which the usual decomposition of mse into the sum of ESB (the first term) and variance (the second term) is shown. This decomposition of the mse into a bias term that is independent of measurement error and a variance term that is independent of the quantity being
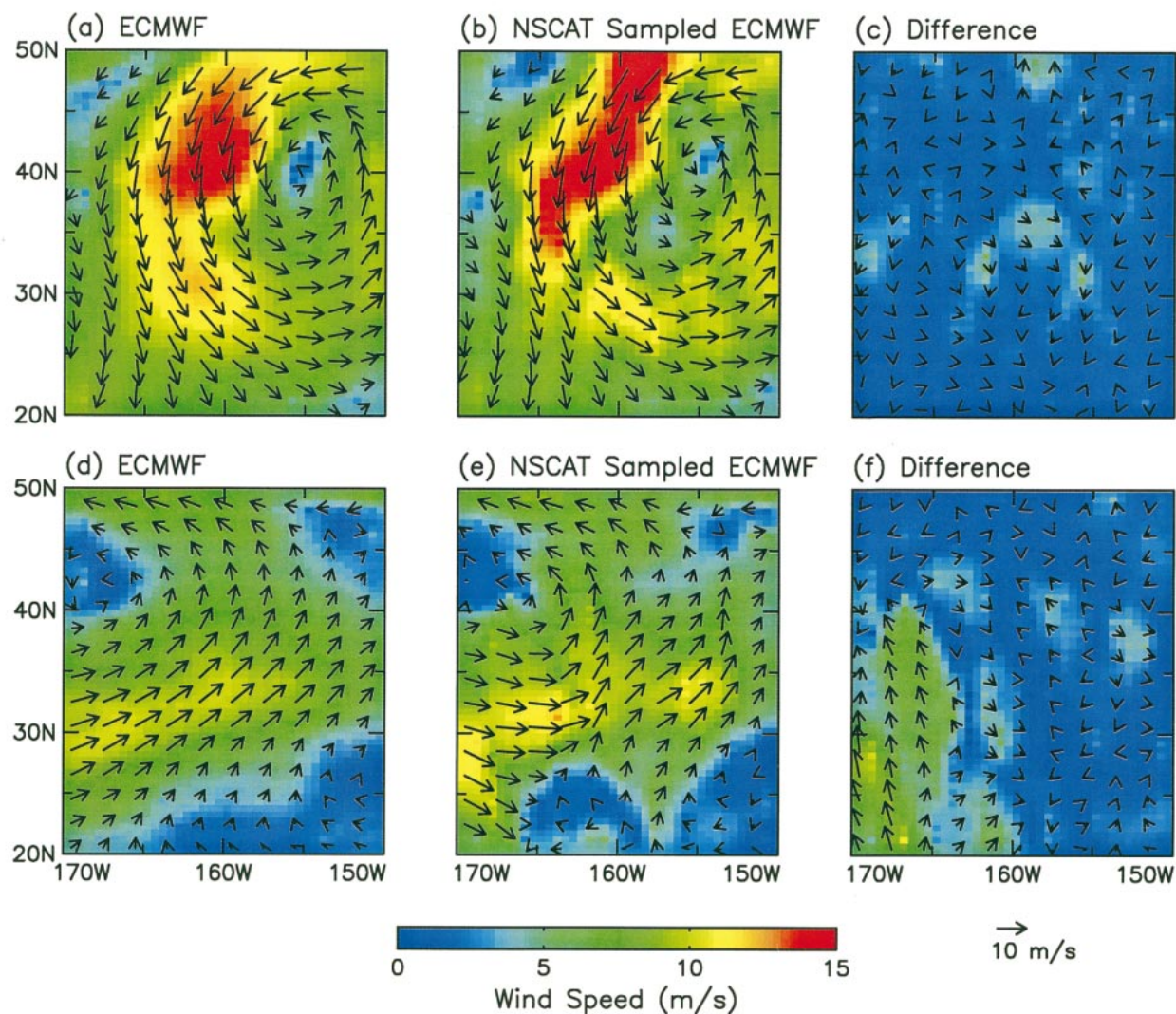
FIG. 2. Maps of vector wind and magnitude of the vector wind made using loess smoothing to retain scales longer than 200 km and 4 days at reference day 45 from (a) ECMWF analyzed surface wind fields, (b) NSCAT-subsampled ECMWF model analyses, and (c) the difference between them. Respectively (d), (e), and (f) are the same, but at reference day 55. Component wind estimates are on a $1° \times 1°$ grid; for clarity wind vectors are drawn at 2° intervals.

estimated makes it a useful tool for the study of sampling errors, which are quantified by the ESB.

The sampling errors associated with four individual scatterometers are investigated here: *ERS-2*, routinely acquiring wind data since April 1996 and preceded by *ERS-1*, which operated from August 1991 through April 1996 (collectively referred to as ERS); NSCAT, carried on the *ADEOS-1* spacecraft, operated from September 1996 through June 1997; ASCAT, to be carried on the European METOP satellite scheduled to launch in August 2003; and SeaWinds, currently operating on board the QuikSCAT spacecraft, launched in June 1999 (referred to here as QuikSCAT). A SeaWinds instrument is also scheduled to be launched on *ADEOS-2* in November 2000 (henceforth referred to as SeaWinds) and forms the basis for the two tandem-mission scenarios considered here: SeaWinds/AS-

CAT and QuikSCAT/SeaWinds. Attention is focused on the geographical region shown in Fig. 1.

This paper is organized as follows. Section 2 describes in detail the sampling patterns of the six scatterometer scenarios. In section 3, the derivation of the methodology underlying the use of the ESB is outlined, along with a brief discussion of the effects of measurement errors. Section 4 describes the sampling errors for the six cases. Details of the ESB calculation, including refinements and extensions of previous applications of the formalism are in the appendix, along with a summary of the relative importance of sampling and measurement errors.

2. Scatterometer sampling

Each of the scatterometers considered here is carried on board a spacecraft placed in an exact repeat, sun-
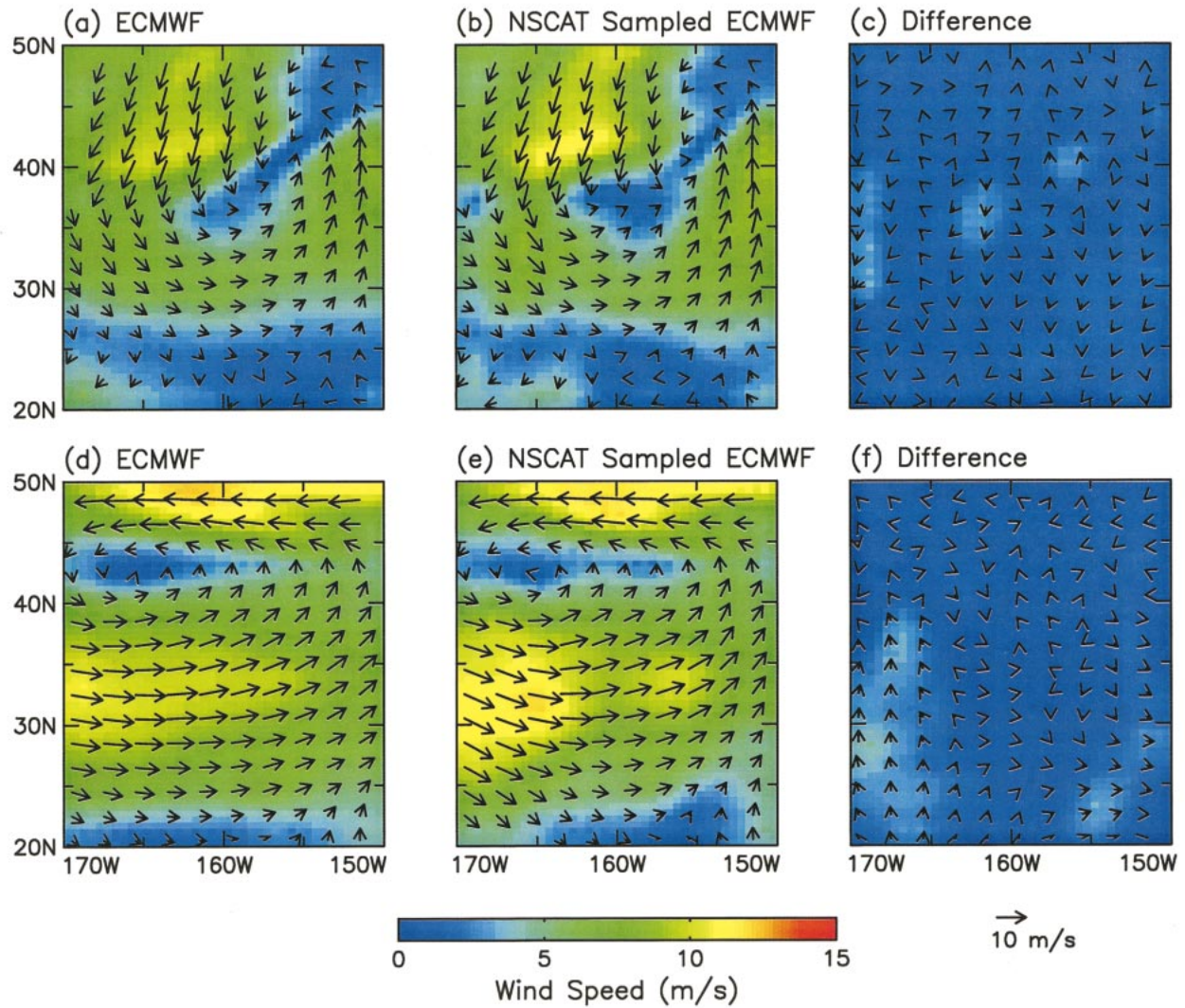
FIG. 3. The same as Fig. 2, except using loess smoothing to retain scales longer than 600 km zonally, 200 km meridionally and 10 days.

synchronous orbit. Measurements of wind speed and direction are made in swaths that parallel the ground track of the spacecraft. As shown in Fig. 1, the spatial sampling density is nearly uniform within each measurement swath. For this study, measurements were assumed to be separated by 50 km in both the along-track and across-track directions. The scatterometer instruments on board the ERS satellites obtain wind measurements in a single 500-km-wide swath beginning 225 km to the starboard side of the ground track (or nadir) (Fig. 1a). NSCAT (Fig. 1b) acquired data in dual 600-km-wide swaths separated by a 330-km nadir gap. AS-CAT (Fig. 1c) will be another dual-swath instrument with swath widths of 550 km separated by a 600-km nadir gap. QuikSCAT (Fig. 1d) has a single 1600-km-wide swath centered on the ground track.

In contrast to the nearly uniform within-swath sampling, the swaths themselves form a relatively sparse space–time pattern (Fig. 4) that depends on swath width

and mission orbital parameters. ERS has an exact repeat period of 35 days and a ground track (or nodal) spacing of about 1.5° of longitude at the equator. NSCAT repeated every 41 days and had a correspondingly smaller nodal spacing of 0.62°. ASCAT will have an exact repeat of 5 days and a nodal spacing of 5.1°, while the orbits for QuikSCAT and SeaWinds have 4-day exact repeats and nodal spacings of 6.3°. The complicated juxtaposition of densely sampled swaths makes describing and understanding scatterometer sampling a difficult undertaking.

It is informative to quantify sampling density variations with time and latitude for each of the scatterometer mission scenarios. One measure of the space–time sampling density is the percentage of $1° \times 1°$ bins that are sampled at least once during a fixed period. This percentage was determined for specified time intervals and the longitude range 150°–170°W for each degree of latitude between the equator and 60°N. The fractional cov-
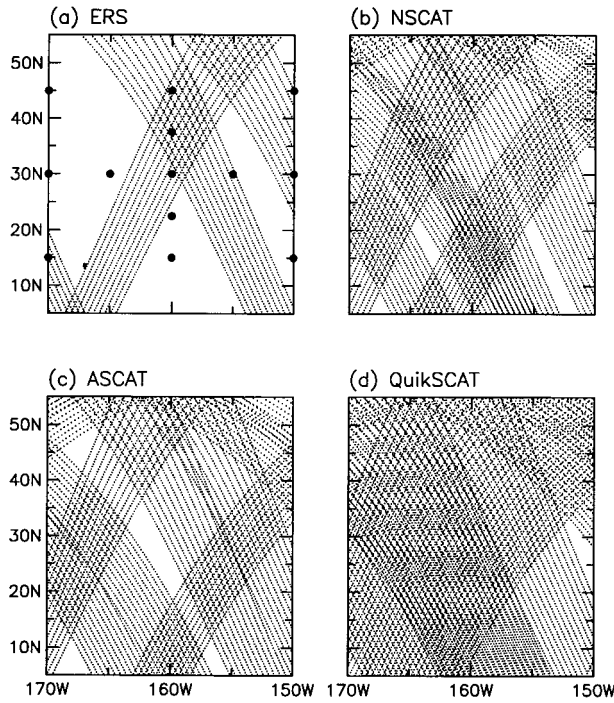
FIG. 4. Measurement locations from a 48-h period over the North Pacific Ocean for each of the single-scatterometer missions. (a) ERS, (b) NSCAT, (c) ASCAT, and (d) QuikSCAT. The large dots in (a) mark the locations where the empirical autocorrelation functions shown in Fig. 11 were calculated.

erages were averaged over the nonoverlapping time intervals contained in an 80-day period. The percent coverages for the six scenarios (Fig. 5) show the progressive increase in sampling density from the narrow, single swath of ERS, through the dual-swath instruments to the single wide swath coverage of QuikScat. Tandem missions increase spatial coverage dramatically and reduce the strong midlatitude variation in coverage associated with the single-instrument scenarios.

The complex spatial–temporal distributions of the measurements for the six scenarios are illustrated in Fig. 6. Measurements at 10°, 25°, 40°, and 50°N are shown in time–longitude sections covering a 20-day period for the longitude range 150°–170°W (the continuous horizontal lines in Fig. 6 result from essentially simultaneous measurements across a swath). As a measurement swath traverses the study area (Figs. 1 and 4), the longitude of the swath steadily changes with latitude, juxtaposing the measurements with those from both ascending and descending swaths that occur at other times. This latitudinally varying combination of sampling times results in the different temporal sampling intervals apparent in Fig. 6. For example, consider the two ERS measurement swaths closest to day 38 in the far left panel of Fig. 6a. At 10°N, these swaths are centered at about 167°W (the later swath) and 154°W (the earlier swath). At 25°N, the later swath has shifted east to 164°N and the earlier swath west to 157°W. At 40°N,
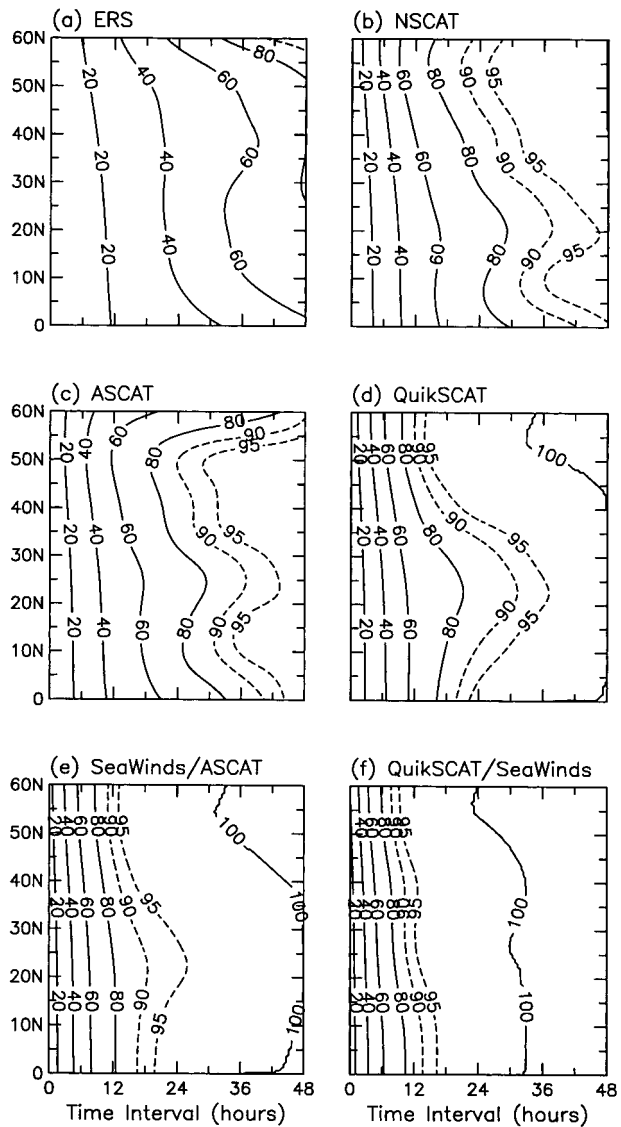

FIG. 5. The percentage of the 1° × 1° bins along each latitude within the longitude range 150°–170°W that contain at least one measurement during the time interval indicated along the abscissa. For each time interval, the percent cover was determined from the average over all nonoverlapping time intervals contained in an 80-day period.

the two swaths have converged in longitude near 160°W; at 50°N, the continued eastward and westward shifts have nearly eliminated longitudinal overlap. The overall result of these shifts and overlaps is temporal sampling that can change radically with both latitude and longitude.

A common feature in the sampling of all of the individual instruments is "burst" sampling in time, where several closely spaced data points occur, followed by a longer data gap, another burst of samples, and so on. For example, QuikSCAT sampling at 10°N, 160°W (Fig. 6d, left panel) exhibits a pattern of two measurements separated by 12 h followed by a 24-h gap, in turn fol-
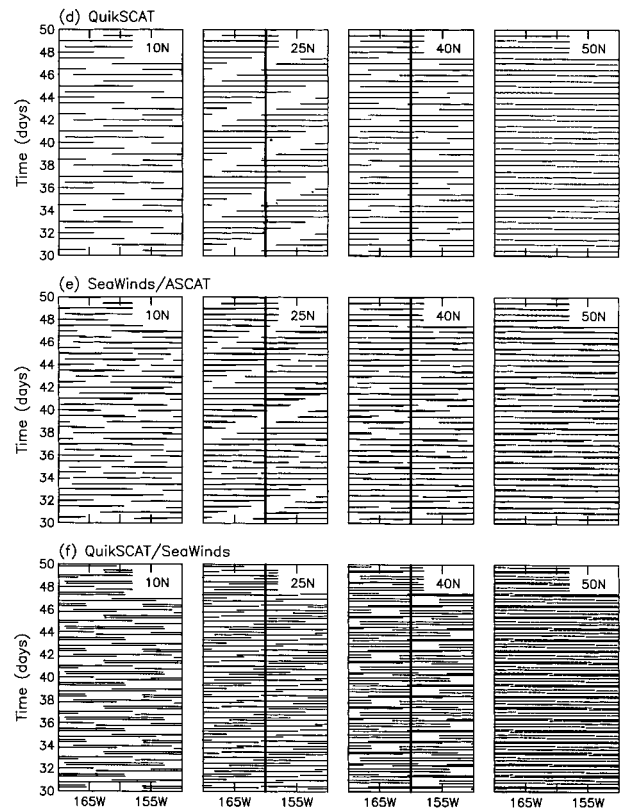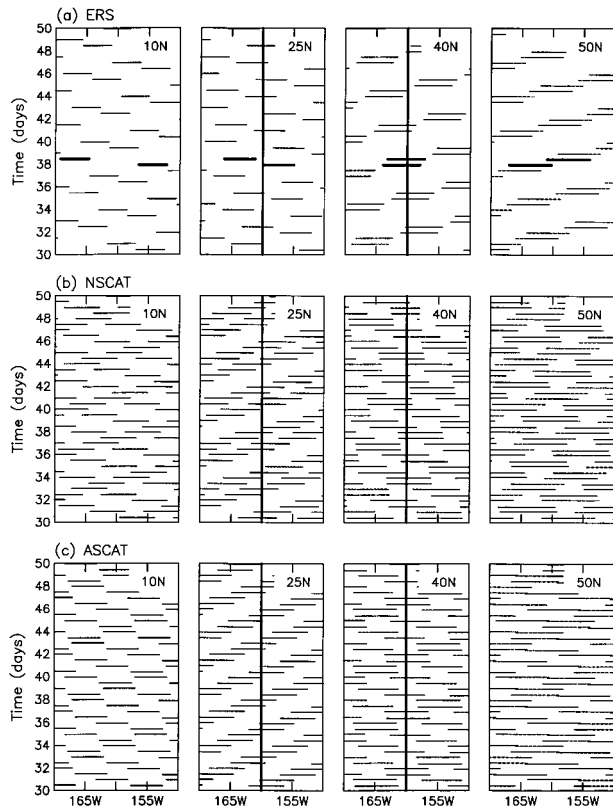
FIG. 6. Measurement locations at 10°, 25°, 40°, and 50°N, plotted in a time–longitude section for the scatterometer scenarios (a) ERS, (b) NSCAT, (c) ASCAT, (d) QuikSCAT, (e) SeaWinds/ASCAT, and (f) QuikSCAT/SeaWinds. The solid vertical lines show the longitude of the error time series in Fig. 15. The measurements closest to day 38 in (a) are denoted by thick lines.

FIG. 6. (*Continued*)

lowed by four measurements separated by 12 h and another 24-h gap. At 25°N, (second panel) the temporal sampling has changed to bursts of 6 measurements, again separated by 12 h, followed by gaps of 48- and 36-h duration, respectively. Similar patterns of burst sampling by the single scatterometers are visible in all of the panels of Fig. 6 except at 50°N for QuikSCAT, where the temporal sampling is nearly uniform.

Figures 6e and 6f show the sampling for the tandem scenarios. The combination of SeaWinds and ASCAT improves data coverage over QuikSCAT, but the swaths from these two instruments are only slightly offset in both time and space, limiting the improvement in coverage. There are still relatively long gaps of a day or more at 10°, 25°, and 40°N. At 50°N the temporal sampling is nearly uniform, but more longitudinal variation in the sampling is apparent than for QuikSCAT at the same latitude. The effect of the different 4- and 5-day exact repeats of SeaWinds and ASCAT is most apparent in the sampling pattern for the combined SeaWinds/ASCAT scenario at 25°N.

The combination of QuikSCAT and SeaWinds shows a marked increase in coverage over an individual SeaWinds instrument. The swaths from the two instru-

ments with the same 4-day repeat provide complementary spatial and temporal coverage as each instrument effectively fills in data gaps left by the other. There are no data gaps longer than a day.

The temporal sampling characteristics of the six scenarios are summarized in Figs. 7 and 8. Figure 7 presents the mean revisit interval (or time between successive measurements) for 1° × 1° bins, calculated at each latitude over the longitude range 150°–170°W. The mean revisit interval is a convenient statistic for characterizing
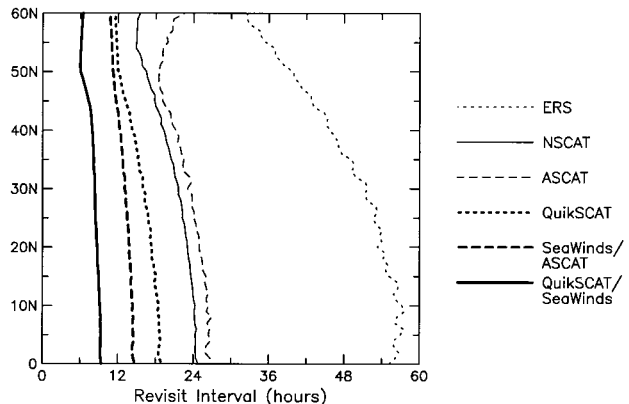

FIG. 7. Mean revisit intervals for measurements in 1° × 1° bins along each latitude within the longitude range 150°–170°W.
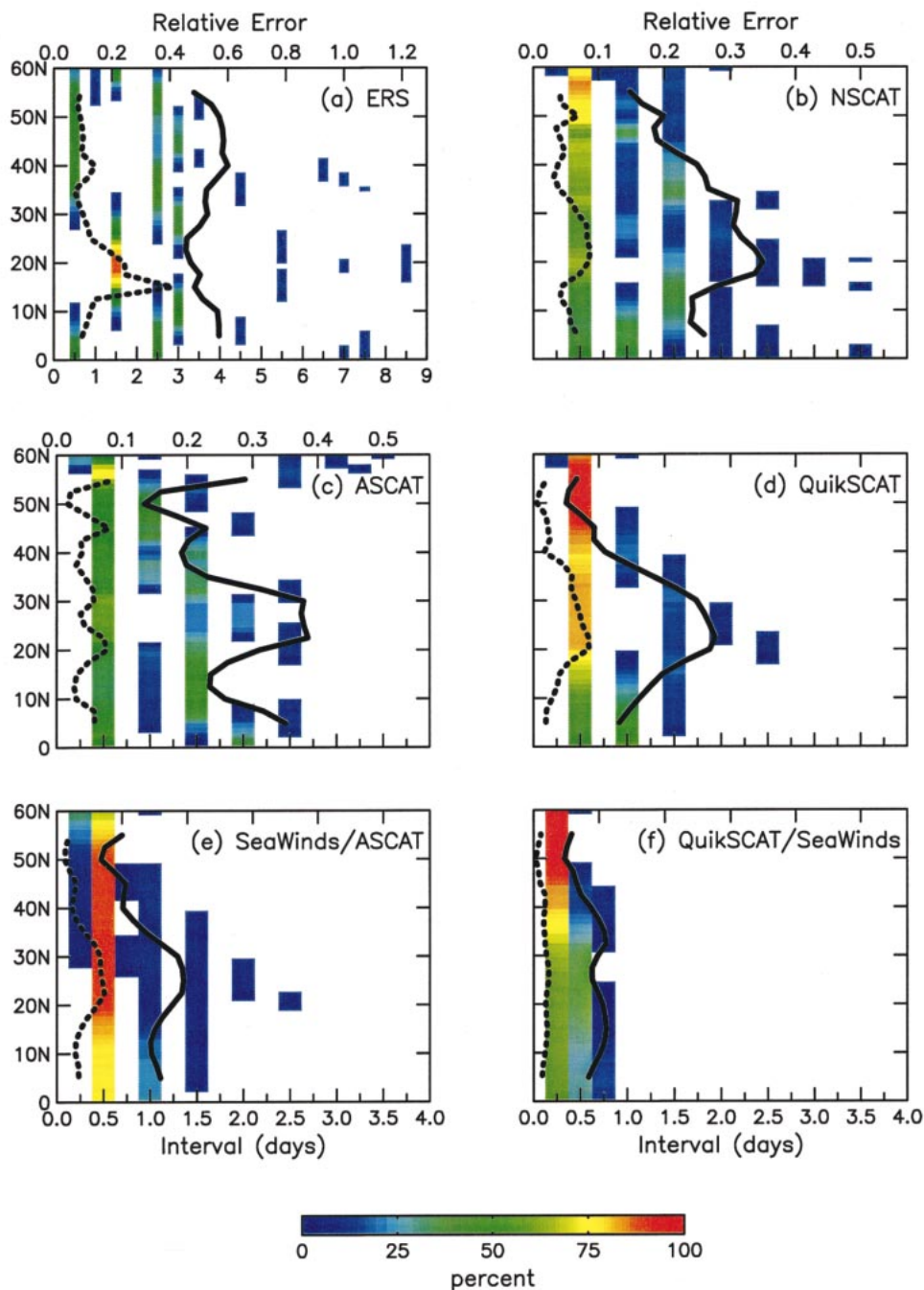
FIG. 8. Latitude–time histograms of revisit intervals for measurements in $1° \times 1°$ bins along each latitude within the longitude range 150°–170°W. For each histogram, the latitude bin size is 1° and the time bin size is 6 h. Time–latitude bins with no observations are displayed as white. (a) ERS, (b) NSCAT, (c) ASCAT, (d) QuickSCAT, (e) SeaWinds/ASCAT, and (f) QuikSCAT/SeaWinds. The solid and dotted lines are, respectively, the mean and standard deviation of the sampling errors calculated as described in section 4. The scale for the time intervals is given by the bottom axis; the scale for the relative errors is given by the top axis. Note the expanded horizontal scale in (a).

scatterometer sampling, but is incomplete because of the burst sampling discussed above. The temporal sampling at each longitude is characterized by a wide range of revisit intervals. The means in Fig. 7 are only the first moments of the revisit interval distributions. Histograms of revisit intervals provide a more comprehensive description of temporal sampling (Fig. 8). For example, the complicated QuikSCAT sampling at 10°N

(Fig. 6d) leads to three dominant sampling intervals ($\sim$12, 24, and 36 h). At 25°N there are still three distinct revisit intervals, but they have shifted to the 12-, 36-, and 48-h intervals noted previously in Fig. 6d.

Figure 8 reveals the complex latitudinal dependence of the revisit interval histograms. With the exception of ERS between about 12° and 26°N, the temporal sampling of all of the scenarios is dominated by ≤12 h intervals at all latitudes, a reflection of the sun-synchronous orbits. However, some latitude ranges are characterized by much longer revisit intervals for some missions. ERS has the most latitudinally variable distribution of revisit intervals, as well as the longest gaps. NSCAT and ASCAT both have extensive sampling at 36- and 48-h intervals, with some data gaps as long as 3.5 days. QuikSCAT sampling rarely has gaps longer than 36 h (the regions near 25°N is unusual in this respect), and none longer than the very few 2.5-day gaps near 20°N. The SeaWinds/ASCAT tandem exhibits 24- and 36-h intervals, is concentrated about 12-h intervals and adds limited sampling at 6-h intervals north of 30°N. QuikSCAT/SeaWinds never has gaps longer than 18 h and, at all latitudes, at least 30% of the sampling is at 6-h intervals. North of 50°N, the temporal sampling for QuikSCAT/SeaWinds is essentially uniform with 6-h intervals.

The results of this section show that, with the exception of ERS, the single scatterometers considered here can provide almost complete spatial coverage over time intervals of 2 days, and at least 50% coverage at 12-h intervals. The tandem missions improve spatial coverage, with SeaWinds/ASCAT covering 80% of the study region in about 12 h and generally more than 95% in under 24 h. QuikSCAT/SeaWinds covers nearly 90% of the region in about 12 h. It will become apparent in later sections that major sampling differences between the scatterometer mission scenarios lie in the details of the temporal distribution of samples, which in turn depend upon measurement swath geometry and orbit parameters.

3. Methodology

a. Expected squared bias

The ESB calculations described and implemented by Schlax and Chelton (1992), Chelton and Schlax (1994), and Greenslade et al. (1997) are extended here. Let $\mathbf{x}$ = (x, y, t) and $\mathbf{s}$ = (k, l, f) be locations in space–time and wavenumber–frequency, respectively, and $h(\mathbf{x})$ a realization of a stationary random function that describes an oceanographic variable of interest (for present purposes, the zonal or meridional component of wind). Then h has variance σ_h^2, Fourier transform $H(\mathbf{s})$, normalized power spectral density $S(\mathbf{s})$, and correlation function $\rho(\mathbf{x})$.

Real instrumental measurements result in N observations of h at the sampling points $\mathbf{x}_j$,

$$g_j = h(\mathbf{x}_j) + \epsilon_j, \qquad j = 1, 2, \ldots, N, \qquad (2)$$

where the ϵ_j are measurement errors, assumed to have zero mean and variance–covariance matrix $\mathbf{V}_{jk} = E[\epsilon_j \epsilon_k]$.

For the purposes of constructing maps of h from the observations g, suppose that a linear, smoothed estimate is calculated at each grid point:

$$\hat{h} = \sum_{j=1}^{N} \alpha_j g_j. \qquad (3)$$

(Without loss of generality, the location of each estimate may be assumed to be at $\mathbf{x}$ = 0, so no locational dependence is inferred for the α_j.) Presumably $\hat{h}$ is a reasonable estimate of an ideal smoothed or filtered version of h,

$$\overline{h} = \int_{-\infty}^{\infty} P^*(\mathbf{s})H(\mathbf{s}) \, d\mathbf{s}, \qquad (4)$$

where the smoother weights α_j are defined by the interpolation algorithm used, $P(\mathbf{s})$ is the transfer function of the smoother or filter yielding $\overline{h}$, and * denotes the complex conjugate. Further defining the equivalent transfer function for $\hat{h}$ as

$$\hat{P}(\mathbf{s}) = \sum_{j=1}^{N} \alpha_j e^{-i2\pi(kx_j+ly_j+ft_j)}, \qquad (5)$$

allows the ESB for $\hat{h}$ as an estimate of $\overline{h}$ to be expressed as

$$E[(\overline{h} - E[\hat{h}])^2] = \sigma_h^2 \int_{-\infty}^{\infty} \|P(\mathbf{s}) - \hat{P}(\mathbf{s})\|^2 S(\mathbf{s}) \, d\mathbf{s}, \qquad (6)$$

where E is the expectation. Unless P and S have special functional forms (see below), evaluation of the three-dimensional integral in (6) is difficult and may be computer intensive [see e.g., the discussion in chapter 4 of Press et al. (1992)].

In their studies, Chelton and Schlax (1994) and Greenslade et al. (1997) used the tricubic-weighted local regression, or loess, smoother of Cleveland (1979) and Cleveland and Devlin (1988) for (3) and compared the estimates so obtained with an ideal low-pass filter

$$P_I(k, l, f) = \begin{cases} 1, & \text{if } \|(k/k_c)^2 + (l/l_c)^2 + (f/f_c)^2\| \le 1 \\ 0, & \text{otherwise,} \end{cases}$$
$$(7)$$

(where k_c, l_c, and f_c are the wavenumber–frequency cutoffs of the filter), resulting in

$$\text{ESB} = \sigma_h^2 \int_{-\infty}^{\infty} \|P_I(\mathbf{s}) - \hat{P}(\mathbf{s})\|^2 S(\mathbf{s}) \, d\mathbf{s}. \qquad (8)$$

Here, $\|P_I(\mathbf{s}) - \hat{P}(\mathbf{s})\|$ is shown schematically as the shaded region in Fig. 9a for a hypothetical one-dimensional loess estimate using the Gaussian weighting described below.
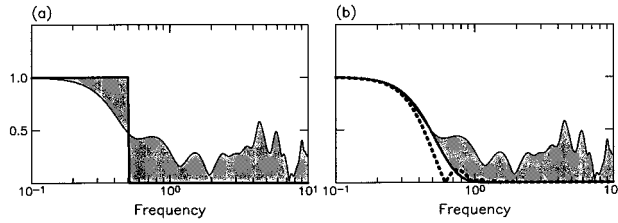
FIG. 9. (a) Transfer function of an ideal low-pass filter $P_I(s)$ (heavy solid line), the equivalent transfer function $\hat{P}(s)$ for a loess estimate from an irregularly spaced dataset (thin solid line), and the difference $\|P_I(s) - \hat{P}(s)\|$ (the shaded region). (b) Transfer functions of an ideal Gaussian-weighted loess estimate $P_G(s)$ (heavy solid line), an ideal tricubic-weighted loess estimate (dotted line), the equivalent transfer function $\hat{P}(s)$ for a loess estimate from an irregularly spaced dataset (thin solid line), and the difference $\|P_G(s) - \hat{P}(s)\|$ (the shaded region).

The ESB provides a measure of how the smoothed estimate (3) has been degraded from the ideal (4), because of inadequate sampling of h by measurements at the points $\mathbf{x}_j$. The difference between the ideal and equivalent transfer functions represents the effects of the sampling error. For the ESB calculation, the difference function is squared and weighted by the amount of spectral energy present at each point in wavenumber–frequency space.

Chelton and Schlax (1994) and Greenslade et al. (1997) used a very restricted space–time grid to describe the variation of ESB for satellite altimeter datasets. The ESB (8) was calculated directly using a Monte Carlo method (a time-consuming procedure) for each estimate. The relatively few evaluations of (8), although burdensome in terms of the required computational effort, were not prohibitive for these studies of altimeter sampling errors.

The scatterometer datasets of interest here do not lend themselves to such a restricted analysis. As seen in section 2, the complex scatterometer sampling requires a more extensive set of ESB calculations to characterize the variability of sampling errors. Direct numerical evaluation of the three-dimensional integral (8) is not feasible. To accommodate the computational demands of this more extensive set of calculations, both the loess estimator and the "ideal" filter to which it is compared were therefore modified.

The goal of the modifications was to choose P and S to be separable functions so that (6) could be written in terms of products of three one-dimensional integrals, while retaining a meaningful definition of the ESB ($\hat{P}$ is always separable). With these changes and a suitable choice of ρ (and hence S), it was possible to obtain a closed-form expression for the ESB and avoid numerical integration entirely. This resulted in a substantial reduction of the computational requirements and allowed the ESB to be calculated on extensive space–time grids. The procedure is outlined in the remainder of this section; details are in the appendix along with a description

of a new method for calculating the loess smoother weights α_j.

The "ideal" filter transfer function (7) was first replaced by the transfer function for a loess estimate made for the continuous case [equivalent to assuming that $h(\mathbf{x})$ is known everywhere]. While it is possible to derive this transfer function for any arbitrarily weighted local regression smoother, the tricubic weighting function commonly used by loess does not provide a separable transfer function. However, as shown in the appendix, if the loess smoother is modified to use a Gaussian weighting function, the transfer function for the corresponding ideal, continuous case is simply

$$P_G(\mathbf{s}) = (1 + \pi^2\|\tilde{\mathbf{s}}\|^2/\sigma)e^{-\pi^2\|\tilde{\mathbf{s}}\|^2/\sigma}, \qquad (9)$$

where $\tilde{\mathbf{s}} = (d_x k, d_y l, d_t f)$ and d_x, d_y, and d_t are the smoother half-spans (appendix). The degree of smoothing is determined by the smoother half-spans; larger half-spans produce smoother estimates. The free parameter σ is chosen to make P_G as close as possible in mean-squared difference to the ideal smoother P_I of Eq. (7) with $(d_x, d_y, d_t) = (k_c^{-1}, l_c^{-1}, f_c^{-1})$. Figure 9b shows the difference $\|P_G - \hat{P}\|$ for the same Gaussian-weighted loess estimate shown in Fig. 9a. Since P_G is defined as a limiting case of the loess smoother being applied here, $\hat{P}$ for a given estimate will, in general, be a better approximation to P_G than to the discontinuous function P_I. ESB calculated using P_I as a reference reflects both sampling error and the degree to which the loess estimator fails to behave as an ideal low-pass filter. ESB calculated with respect to P_G should thus be smaller and more sensitive to sampling errors than ESB based on P_I.

The transfer function for the ideal tricubic loess is also shown as the dotted line in Fig. 9b for comparison with P_G. The ideal tricubic loess smoother rolls off more rapidly than P_G but has larger sidelobes. These tricubic- and Gaussian-weighted transfer functions differ in mean square by less than 3%. The increase in computational efficiency allowed by the Gaussian-weighted smoother more than compensates for this minor difference.

b. Signal autocorrelation function

The ESB calculation requires an assumed form for the signal autocorrelation function, ρ. This function, and its Fourier transform S, define the scales of variability of the wind field and have a direct impact on the ESB reported for a given estimate. Care must be taken in the choice of ρ in order to realistically represent the second-order statistics of the true wind field while also providing for tractable ESB computations.

For this study we require candidate functions for ρ that are positive definite, physically realistic, separable and preferably with a form leading to simple evaluation of (6). Products of the exponentially damped cosine, (e.g., for x, $\exp(-|x/s_x|) \cos[(\pi x)/2L_x]$, where s_x is the decorrelation scale for x and L_x is the zero crossing)

describe well the marginal characteristics of wind fields (Freilich and Chelton 1986) and have been used to analyze sampling errors from scatterometer wind data (Kelly and Caruso 1990). One disadvantage of this representation for ρ is that the surfaces of constant ρ are planar, which is not a particularly realistic feature. Furthermore, while separable, the exponentially damped cosine still requires numerical integration for the evaluation of (6) when using P_G.

The function

$$\rho(x,\, y,\, t;\, s_x,\, s_y,\, s_t,\, L_x,\, L_y,\, L_t)$$

$$= e^{-\|\tilde{\mathbf{x}}\|^2}\left\{1 - \left(\frac{x}{L_x}\right)^2 - \left(\frac{y}{L_y}\right)^2 - \left(\frac{t}{L_t}\right)^2\right\}, \quad (10)$$

where s_x, s_y, and s_t are the decorrelation scales, L_x, L_y, and L_t are the zero crossings, and $\tilde{\mathbf{x}} = (s_x^{-1}x,\ s_y^{-1}y,\ s_t^{-1}t)$, is (as detailed in the appendix) conditionally positive definite, has ellipsoidal level surfaces and allows a closed form expression for (6). One problem with this form for the autocorrelation function is that it describes a wind field that contains preferentially more large-scale variability than is likely to be true, particularly in time. This difficulty may be overcome through the use of a *nested* autocorrelation (Journel and Huijbregts 1978), that is, by expressing ρ as a weighted sum of functions with the form (10) and different decorrelation scales. In the form applied here, (10) does not allow the incorporation of propagating signals.

To determine appropriate values for the parameters of the spatial–temporal autocorrelation functions to be used in this study, a set of empirical temporal autocorrelation functions was calculated from 9.5 months of NSCAT measurements at the locations shown in Fig. 4a [these data have been carefully examined and validated, e.g., Freilich and Dunbar (1999)]. At each location, data from the nine adjacent $1° \times 1°$ latitude–longitude bins was selected and sorted into 0.5-day bins. Using these binned data, the empirical temporal autocorrelation functions for the zonal (u) and meridional (v) wind components were calculated, and are shown in Figs. 10a and b. These figures reveal that the autocorrelation timescale is shorter for v than for u.

Spatial autocorrelation functions are more difficult to estimate from the NSCAT data. Rather than attempting to specify the spatial parameters directly, autocorrelation functions with three sets of spatial parameters were used to investigate the sensitivity of the ESB to the spatial form of the autocorrelation.

A total of four subjectively chosen spatial–temporal autocorrelation functions were considered in this study. Define the short and long timescale autocorrelation functions $\rho_{ts}(x,\, y,\, t)$ and $\rho_{tl}(x,\, y,\, t)$, respectively, both with isotropic spatial parameters $s_x = s_y = 700$ km and $L_x = L_y = 900$ km, and no temporal zero-crossing (i.e., $L_t = \infty$). For ρ_{ts} the temporal decorrelation parameter is $s_t = 0.95$ days, while for ρ_{tl}, $s_t = 5$ days. The space–

time autocorrelation function used for the zonal wind component was

$$\rho_u(x,\, y,\, t) = 0.55\rho_{ts}(x,\, y,\, t) + 0.45\rho_{tl}(x,\, y,\, t),$$

while for the meridional component

$$\rho_v(x,\, y,\, t) = 0.85\rho_{ts}(x,\, y,\, t) + 0.15\rho_{tl}(x,\, y,\, t).$$

Since these functions are spatially symmetric, they may be expressed as functions of $r = \sqrt{x^2 + y^2}$. Overlaid as the heavy lines in Figs. 10a and 10b are $\rho_u(r,\, t)$ and $\rho_v(r,\, t)$, as functions of the temporal lag t, respectively, for $r = 0$. These analytical autocorrelation functions provide a good visual fit to the empirical temporal autocorrelation functions. The temporal decorrelation scales of these functions are quite different. The *e*-folding timescales of ρ_u and ρ_v are 2.3 days and 1.1 days, respectively. For most of the calculations made here, we have used ρ_v to provide a conservative assessment of the impact of sampling errors.

For examining the sensitivity of the sampling errors to the spatial decorrelation scale, autocorrelation functions with short and long spatial ranges, ranges, ρ_{vs} and ρ_{vl} are defined to have the same temporal structure as ρ_v, but spatial parameters s_x, s_y, L_x, and L_y that are respectively half and twice those of ρ_v. Figure 10c displays $\rho_{vs}(r,\, t)$, $\rho_v(r,\, t)$, and $\rho_{vl}(r,\, t)$ as functions of spatial lag r for $t = 0$.

c. Characterization of sampling errors

The studies of Chelton and Schlax (1994) and Greenslade et al. (1997) used the relative expected squared bias RESB $= \mathrm{ESB}/\sigma_h^2$ to quantify the effect of sampling errors on grids of smoothed estimates of sea surface height data. One goal of these studies was to define the "resolution capability" of a given set of altimeter measurements of sea surface height. The resolution capability was defined as the minimum degree of smoothing required to produce grids with errors that were either deemed sufficiently small in magnitude, or exhibited a defined degree of homogeneity, as measured by the mean and variability of the square root of the RESB.

This study pursues the less ambitious goal of simply describing the mean and variability of the relative sampling errors [defined as $(\mathrm{RESB})^{1/2}$] associated with the six scatterometer scenarios described in the preceding sections. The mean and variability of the relative sampling errors of mapped wind components were examined in space and time, and as a function of the applied smoothing. The various spatial–temporal autocorrelation functions defined above were used to demonstrate the sensitivity of sampling errors to the assumed autocorrelation function.

Practical application of the methodology presented here requires the specification of σ_h to convert relative sampling errors into absolute sampling errors. In objective analyses, it is common to remove the mean field and interpolate the residuals. For such applications, it
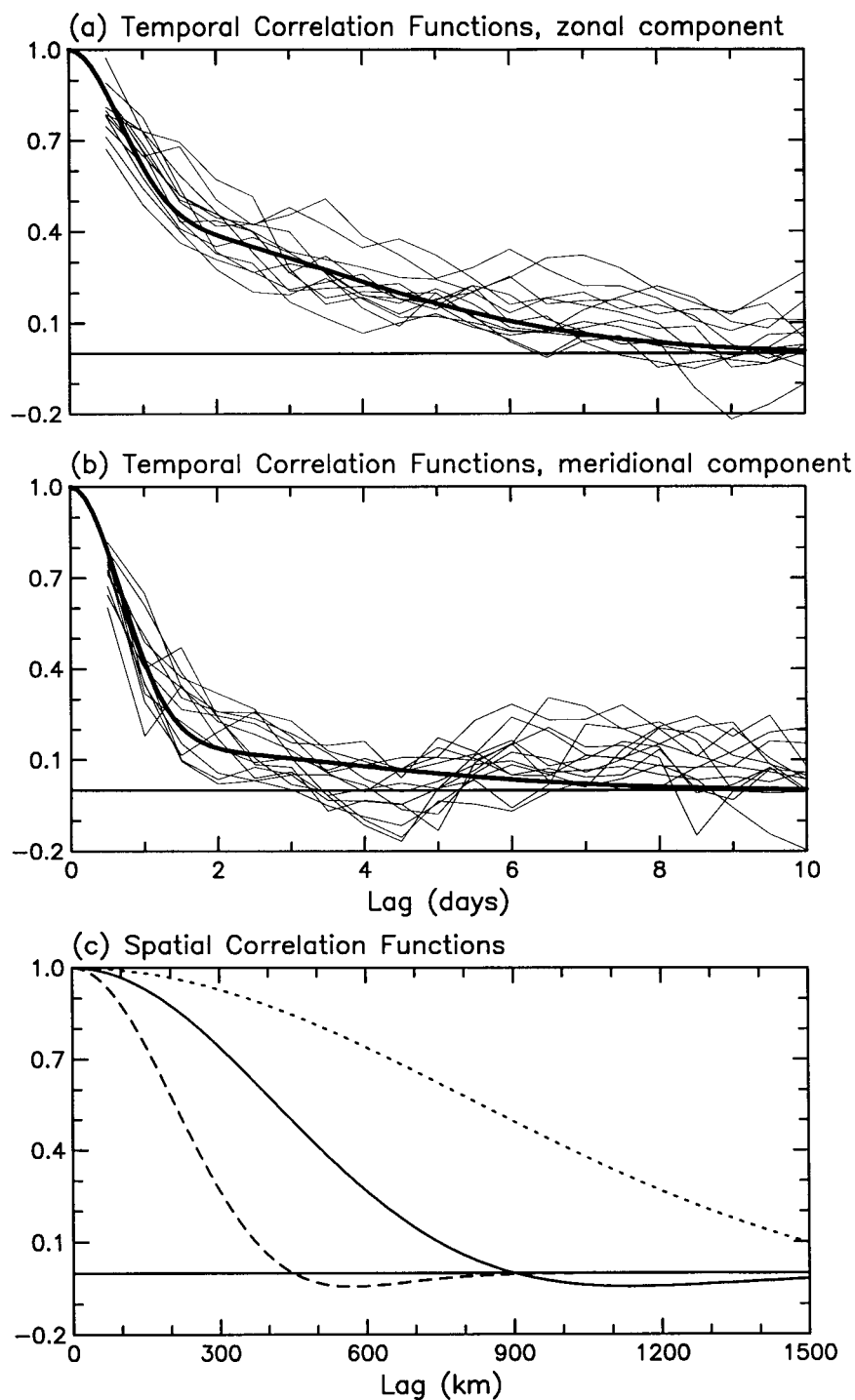
FIG. 10. (a) Empirical temporal autocorrelation functions for the zonal wind component from the 13 locations marked in Fig. 4a (light lines). Overlaid as the heavy line is the analytical space–time autocorrelation function $\rho_u(r, t)$ as a function of temporal lag t for spatial lag $r = x^2 + y^2 = 0$. (b) Same as in (a), except for the meridional wind component, and the space–time autocorrelation function $\rho_v(r, t)$ as a function of temporal lag t for spatial lag $r = 0$. (c) Plots of the space–time autocorrelation functions $\rho_{us}(r, t)$ (dashed line) $\rho_v(r, t)$ (solid line) and $\rho_{ul}(r, t)$ (dotted line) as functions of spatial lag r for temporal lag $t = 0$, where the functions ρ_{us} and ρ_{ul} have the same form as ρ_v, but with spatial decorrelation scales and zero-crossings, respectively, half and twice those of ρ_v.
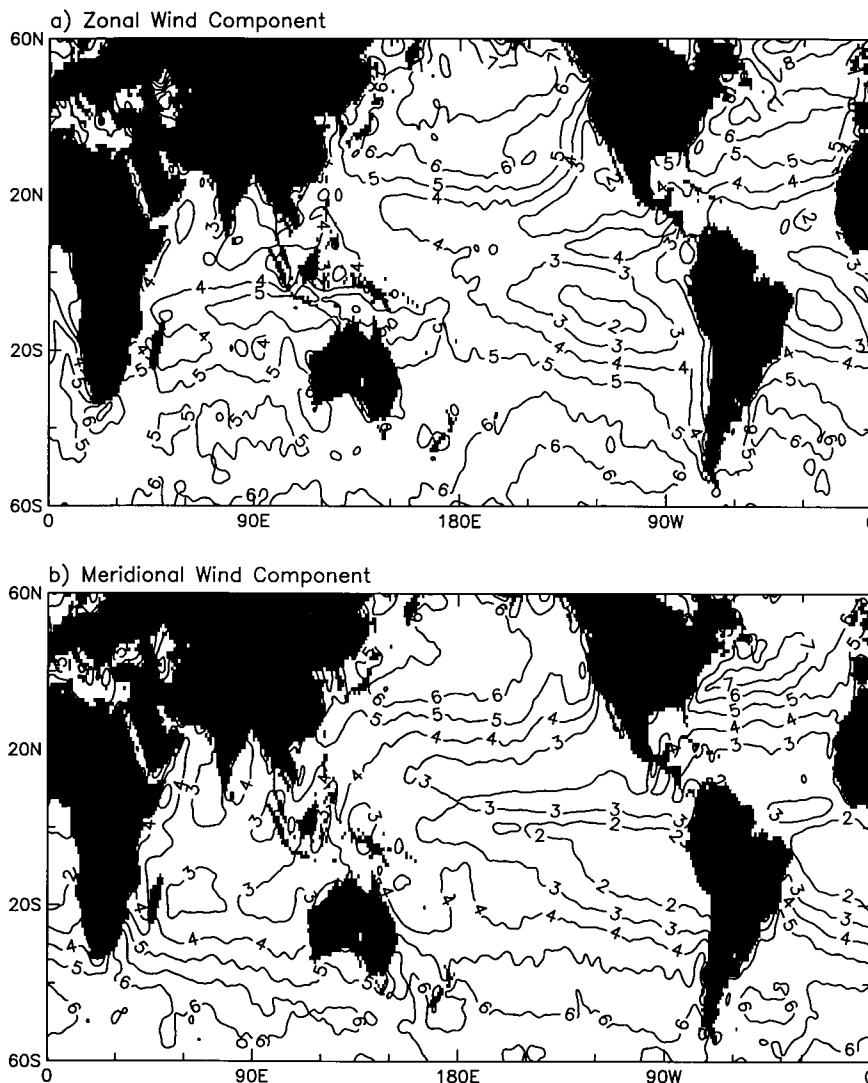
FIG. 11. Standard deviation of (a) zonal wind component and (b) meridional wind component, in m s^{-1}, calculated over 1° × 1° bins from 9.5 months of NSCAT data.

is appropriate to consider the standard deviation of the wind components. Figure 11 shows maps of the standard deviations of the zonal and meridional wind components calculated in 1° × 1° bins using the 9.5 months of NSCAT data. (The presence of ambiguity removal errors will elevate estimates of standard deviation. Comparison with the wind component standard deviations calculated using ECMWF analyzed surface winds suggests that the effect of the ambiguity removal errors is not large for this calculation. See also Freilich and Dunbar 1999.) The standard deviations of both components increase from minimum values near 2 m s^{-1} in the equatorial regions to 6–7 m s^{-1} at higher latitudes, and have global mean values of 5 m s^{-1} and 4.6 m s^{-1} for the zonal and meridional components, respectively. The geographic variation of the wind component standard deviations makes it clear that absolute sampling errors need to be evaluated on a regional basis. For the purposes of comparing absolute sampling errors for the six mission scenarios (section 5) and for comparing measurement with sampling errors (section 3d and the appendix), a 5 m s^{-1} standard deviation is assumed. This value is comparable to the range of wind component standard deviations used by Kelly and Caruso (1990).

d. Variance of the estimates

The second term of Eq. (1) is the variance of the linear estimates,

$$\mathrm{var}(\hat{h}) = E[(\hat{h} - E[\hat{h}])^2] = \sum_{j,k=1}^{N} \alpha_j \mathbf{V}_{jk} \alpha_k. \quad (11)$$

An attempt to describe the nature of error correlations

in scatterometer data is beyond the scope of this paper. Assuming uncorrelated errors (i.e., that **V** is the identity) provides only a lower bound for the variance; correlated errors will lead to larger variances. To estimate the general magnitude of the variance of the linear estimates studied here, Gaussian space–time autocorrelation functions for the errors were assumed. Three cases were considered: uncorrelated errors, correlated errors with a temporal decorrelation of 50 min (reflecting an assumption that errors from different orbits are uncorrelated), and isotropic spatial decorrelation of 100 km, and correlated errors with the same temporal decorrelation and 200-km spatial decorrelation. The error standard deviation $\sigma_\epsilon = (E[\epsilon^2])^{1/2}$ was assumed to be 1 m s^{-1} (Freilich and Dunbar 1999). Equation (11) was evaluated for Gaussian-weighted loess smoothers with three levels of smoothing: $d_x = d_y = 1°$, $d_t = 2$ days; $d_x = d_y = 2°$, $d_t = 4$ days; and $d_x = d_y = 3°$, $d_t = 12$ days. Discussion of the results is deferred until the appendix for comparison with a summary of the sampling errors.

4. Scatterometer sampling errors

Figures 12, 13, and 14 display relative sampling errors calculated for the six scatterometer scenarios for specific spatial and temporal smoothing and specific estimation times. These figures show maps of (RESB)$^{1/2}$ using the meridional wind component space–time autocorrelation function ρ_v, and thus are representative of the errors expected in maps of the meridional wind component. Because of the shorter decorrelation scale of ρ_v, these errors will be larger than those associated with ρ_u (see Fig. 15). All spatial smoothing was isotropic; the spatial smoothing can thus be described by the single parameter $d_s = d_x = d_y$. For all of the calculations presented in this section, a sufficient number of sampling locations was used so that the error estimates were not contaminated by boundary effects. The times referred to in these and the following figures are the same as those used on the ordinates in Fig. 6.

Figure 12 shows the errors for each mission scenario on day 40 for loess estimates with $d_s = 2°$ and $d_t = 4$ days. The error patterns are complex and heterogeneous. The diagonal patterns and diamond-shaped areas correspond to swath boundaries (Fig. 4). Figure 13 shows the errors 2 days later. The errors for all six scenarios have magnitudes and patterns similar to those observed in Fig. 12, but with longitudinal shifts of the various error maxima and minima. Figures 12 and 13 illustrate that sampling errors generally vary both spatially and temporally for a given combination of smoothing parameters.

The latitudinal variations of sampling errors for estimates with $d_s = 2°$ and $d_t = 4$ days are summarized by the curves superimposed on the revisit interval histograms in Fig. 8. Errors were calculated at 2.5° intervals between 5° and 55°N, at 1° intervals between 150° and 170°W, and at 1-day intervals between days 30 and 50. The means and standard deviations of these errors at each latitude reflect the overall level of relative sampling error and its variation over time and longitude. The variations of both the means and the standard deviations of the errors are strongly correlated with the latitudinal variations of the revisit intervals. Increases of the error means and standard deviations occur when there is a shift in the sampling toward longer revisit intervals (i.e., more or longer data gaps in time). The superior performance of QuikSCAT/SeaWinds (Fig. 8f) over the other scenarios results primarily from the uniform, frequent temporal sampling provided by the combination of those two instruments.

Figure 14 shows the errors for the region on day 40, but for significantly smoother maps, $d_s = 3°$, $d_t = 12$ days. The errors for all six scenarios are smaller and less heterogeneous than those shown in Figs. 12 and 13. The diagonal patterns so clearly visible in Fig. 12 are only subtly apparent in Fig. 14. More prominent are isolated local error extrema (e.g., along 50°N for NSCAT, 45°N for ASCAT, and 25°N for QuikSCAT/SeaWinds) and the latitudinal banding of the errors.

The relative importance of temporal versus spatial sampling is evident from Fig. 15, in which the relative sampling errors at 160°W for each of the six scenarios are plotted as functions of time, for 25°N (left panel) and 40°N (right panel), and smoothing parameters $d_s = 2°$ and $d_t = 4$ days. (The heavy solid lines in the middle panels of Fig. 6 show the longitudes where these estimates are located.) The error was calculated using each of the four space–time autocorrelation functions described in section 3. Error values based on the autocorrelation functions ρ_{vs}, ρ_v, and ρ_{vl} are all plotted as solid lines in Fig. 14, while the errors calculated using the longer autocorrelation timescales from ρ_u are plotted as dotted lines. With the exception of ERS at 25°N and day 36.5, the three solid lines in all of the panels of Fig. 15 do not differ from one another by more than 0.1. The errors for this degree of smoothing are thus insensitive to the large difference in the assumed wind spatial variability represented by the three autocorrelation functions ρ_{vs}, ρ_v, and ρ_{vl}. The spatial coverage of each of the six scenarios is apparently sufficient to resolve even the shortest spatial scales represented by ρ_{vs} when smoothed with $d_t = 4$ days. The errors are, however, sensitive to a change in the temporal scales, (apparent from the fact that the dotted lines are lower than the solid lines in every panel of Fig. 15). This decrease in error resulting from using ρ_u rather than ρ_v is generally less than 0.1 for all six scenarios. The reduction of the error with the increase in temporal decorrelation scales from 1.1 days to 2.3 days shows that the scatterometer datasets are better able to resolve the longer timescales represented by ρ_u.

Figure 15 in conjunction with Figs. 6 and 8 also shows how sampling errors respond to spatial and temporal changes in sampling. Consider the case of ERS (Figs. 6a, 8a) at 25°N with respect to sampling changes over
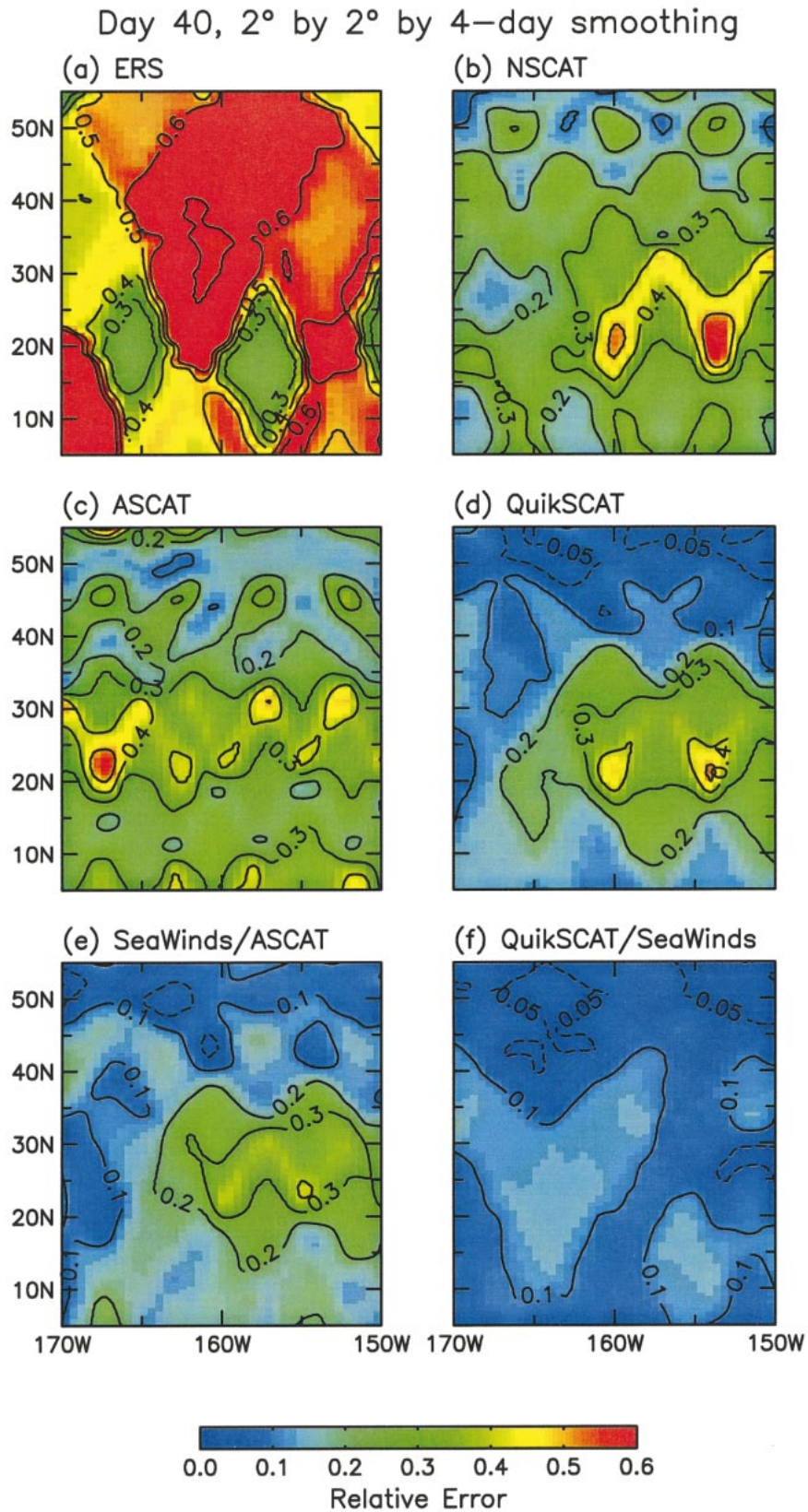
FIG. 12. Relative errors on day 40 for loess estimates assuming the space–time autocorrelation function ρ_v and half-spans $d_x = 2°$, $d_y = 2°$, and $d_t = 4$ days for (a) ERS, (b) NSCAT, (c) ASCAT, (d) QuikSCAT, (e) SeaWinds/ASCAT, and (f) QuikSCAT/SeaWinds.
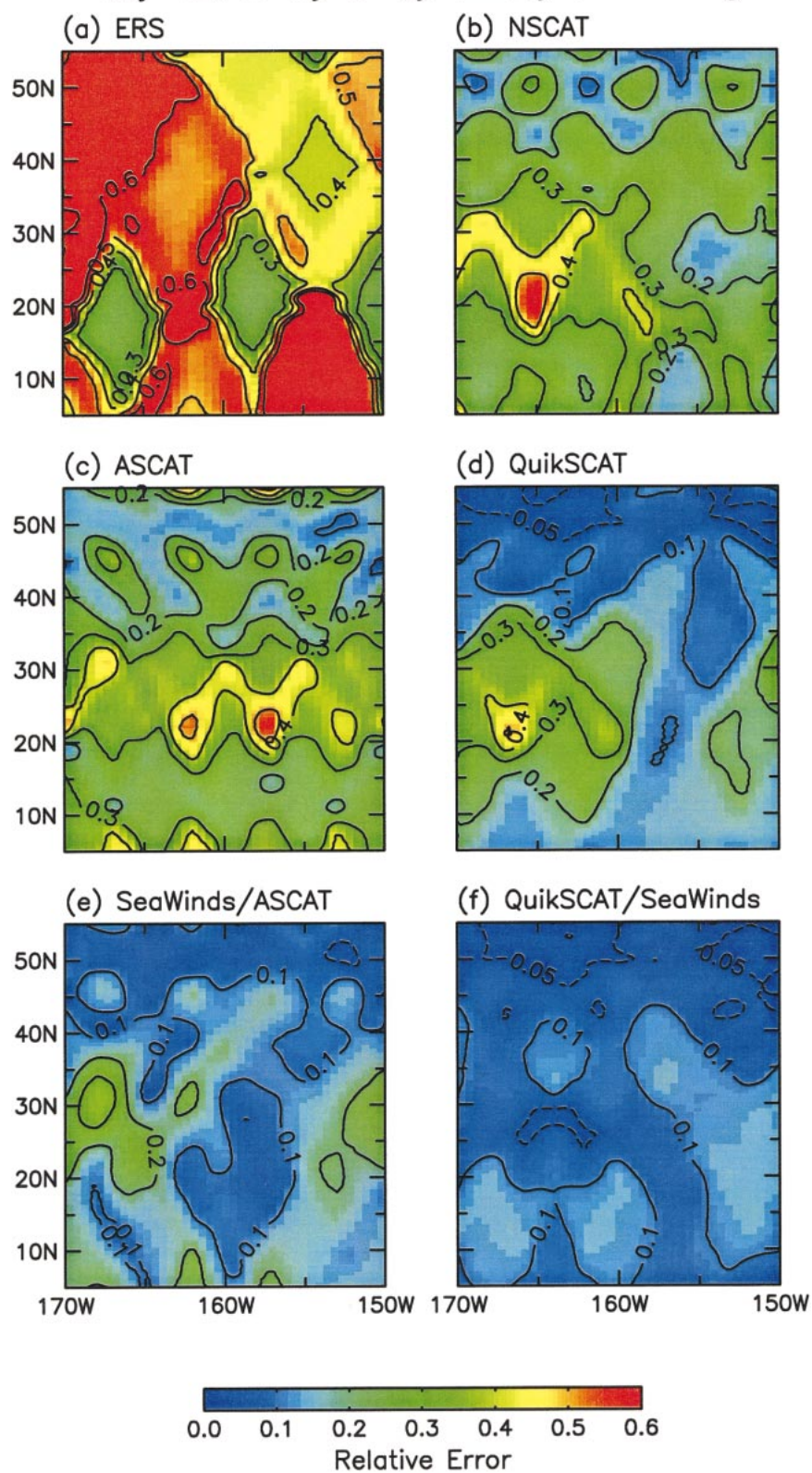
FIG. 13. The same as Fig. 12 except for day 42.
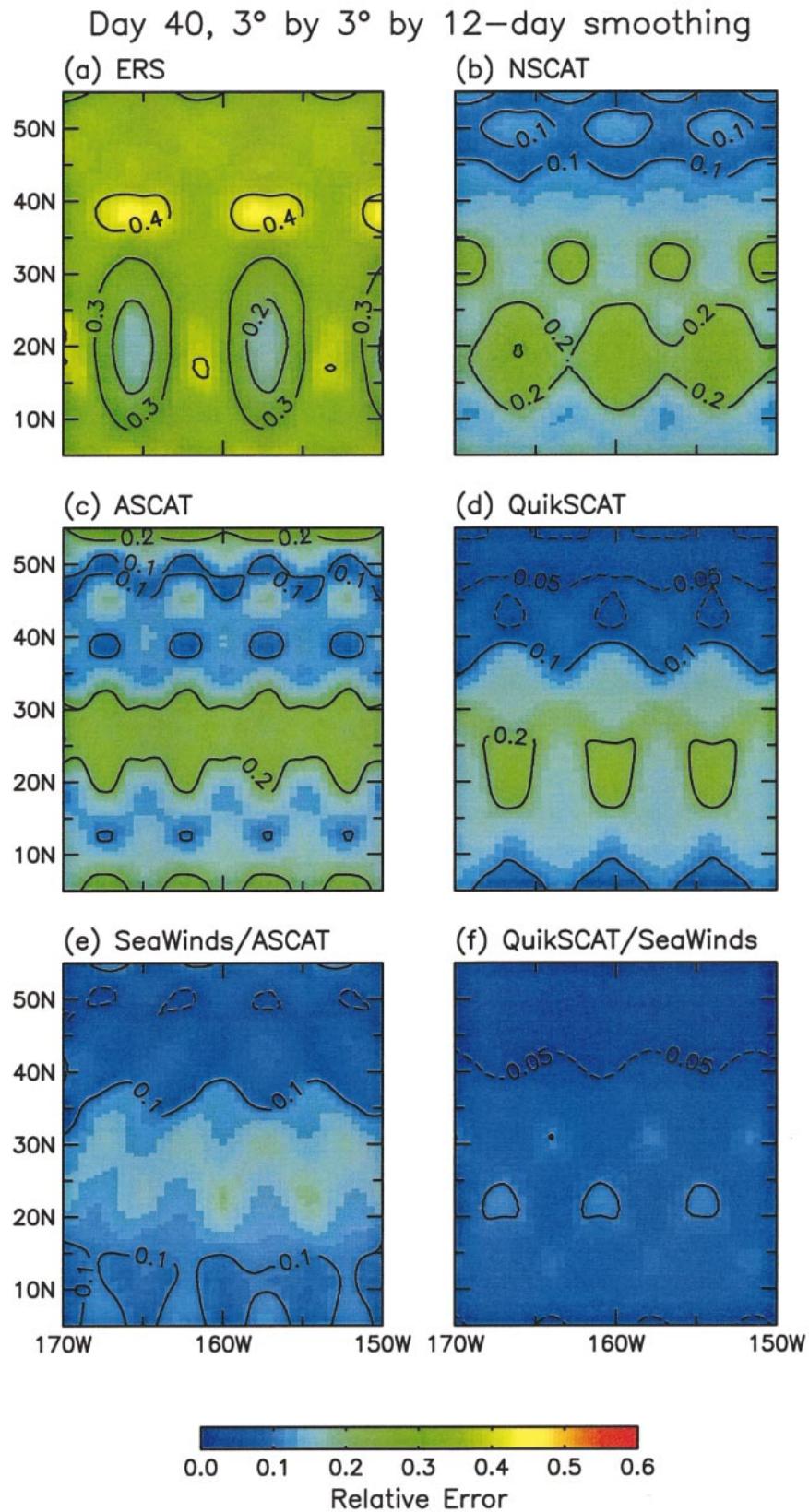
Day 40, 3° by 3° by 12-day smoothing

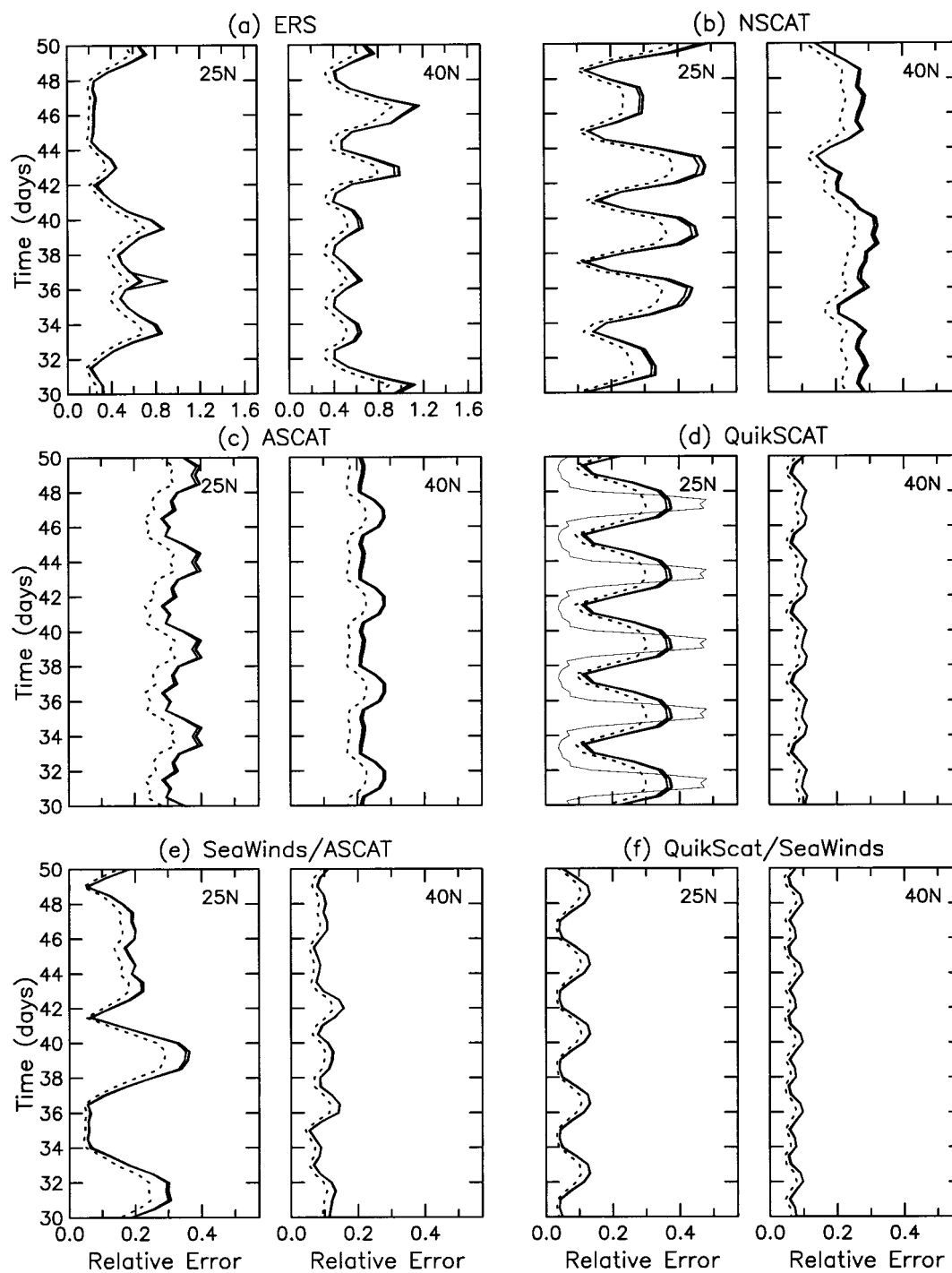FIG. 14. The same as Fig. 12 except for loess estimates with half-spans $d_x = 3°$, $d_y = 3°$, and $d_t = 12$ days.

FIG. 15. Relative errors as a function of time at 160°W for 25°N (left panels), and 40°N (right panels) for loess estimates with half-spans $d_x = 2°$, $d_y = 2°$, and $d_t = 4$ days assuming the space–time autocorrelation functions ρ_v, ρ_{vs}, ρ_{vl} (solid lines), and ρ_u (dotted line) for (a) ERS, (b) NSCAT, (c) ASCAT, (d) QuikSCAT, (e) SeaWinds/ASCAT, and (f) QuikSCAT/ SeaWinds. Note the larger error scale in (a). The additional thin solid line in the left panel of (d) shows sampling errors for $d_x = 2°$, $d_y = 2°$, and $d_t = 1.5$, assuming ρ_v.

time at 160°W. The basic sampling interval is 18 h, with occasional longer gaps of 2.5, 3, and 5.5 days. The errors (Fig. 15a, left panel) are small when measurement swaths lie substantially within the span of the smoother, and larger when the data density is low. The largest difference between the errors found using ρ_v, ρ_{vs}, and ρ_{vl} occurs at day 36.5, where the measurement swaths lie farthest from the estimation location.

As noted in section 2, the nature of the ERS temporal sampling at 40°N is very different. The swaths are separated by alternating intervals of 12 h and 2.5 days, with occasional longer intervals of 3, 3.5, and 6.5 days (Fig. 8a) and this is reflected by the errors. The errors oscillate with a 3-day period with relative minima centered where the swaths are separated by 12 h, and relative maxima centered on the longer 2.5-day intervals that intervene. The magnitudes of the maxima increase where there are wider longitudinal gaps between the swaths (near days 30, 43, and 46). The mean error over time is greater at 40° than at 25°N because the burst sampling at the higher latitude is less able to resolve some of the timescales represented by the autocorrelation functions used here.

Figures 6 and 15 reveal a close correspondence between the variation of errors and the temporal sampling for the other five scenarios as well. The 5- and 4-day exact repeat periods of ASCAT and QuikSCAT are reflected by the periodic variation of the errors in Figs. 15c and 15d. For the SeaWinds/ASCAT scenario at 25°N (Figs. 6e and 15e), the relatively long-period variation in sampling results in a similar temporal variation in the errors. The QuikSCAT/SeaWinds scenario has errors with 4-day periodicity, in accordance with the 4-day exact repeats of the two individual scatterometers comprising the scenario.

QuikSCAT at 25°N (Figs. 6d and 15d) provides a clear example of how the errors are small during times of high data density that occur during a burst of sampling, and larger during the longer gaps. The wind field is sometimes very well sampled and resolved, but the sampling errors have high temporal variability. The burst sampling can lead to the apparently paradoxical result that less smooth estimates can have lower mean error than smoother estimates. For example, the errors for estimates with for $d_s = 2°$, $d_t = 1.5$ days (shown as the thin solid line in the left-hand panel of Fig. 15d) have a mean of 0.18, while the estimates for $d_s = 2$, $d_t = 4$ days have a mean of 0.27. The trade-off for this locally high resolution is that the variability of the less smooth estimates (0.17 standard deviation) is significantly higher than that for the smoother estimates (0.1).

The preceding calculations provided an indication of the spatial and temporal variability of scatterometer sampling errors for a specific set of smoothing parameters (the half-spans d_x, d_y, and d_t of the loess smoother used here) and show how those errors depend on the space–time autocorrelation of the wind field. Sampling errors also depend on the degree of smoothing, that is, upon the space–time smoothing parameters. To quantify

this dependence, relative sampling errors were calculated for estimates on a space–time grid, for spatial half-spans from $d_s = 1°$ to $d_s = 4°$ and for temporal half-spans ranging from $d_t = 1$ day to $d_t = 15$ days. The space–time grid extended from day 30 to day 50 at daily intervals and from 150° and 170°W at 1° intervals along 10°, 25°, 40°, and 50°N. Based on the temporal and spatial variation of the errors observed in Figs. 12–15, we believe that this grid is sufficient to describe the dependence of the space–time variation of sampling errors on the degree of smoothing applied, for estimates made over the study region. The space–time autocorrelation function ρ_v was used for this calculation. As shown in Fig. 15, the errors associated with ρ_v are always somewhat greater than those for the autocorrelation function ρ_u, and thus provide a conservative estimate of the sampling errors for both wind components. The results of this calculation are summarized in Fig. 16 where the means and standard deviations of the errors are contoured as functions of d_s and d_t.

ERS has the largest and most variable errors. NSCAT and ASCAT have similar mean errors, but ASCAT has higher overall error variability than NSCAT. QuikSCAT mean errors are less than those for both NSCAT and ASCAT. For d_s less than 3° and d_t less than 4 or 5 days, QuikSCAT errors are less variable than either NSCAT or ASCAT, but outside of that range the standard deviation of the QuikSCAT errors is greater than those for ASCAT and NSCAT. The mean errors for SeaWinds/ASCAT are only marginally lower than those for QuikSCAT, but the error standard deviation for the tandem scenario is reduced by 0.02–0.03 overall. Quik-SCAT/SeaWinds has the lowest error mean and standard deviation, never exceeding 0.07 and 0.04, respectively.

For all six scenarios the mean and variability of the relative sampling errors is more sensitive to the choice of d_t than to d_s.

The local mean error minima and corresponding error standard deviation maxima at the plot origins for NSCAT, QuikSCAT, and SeaWinds/ASCAT are the result of the phenomenon described in Fig. 15d, for QuikSCAT; locally dense sampling allows locally high resolution of short timescales and correspondingly low mean error, but high overall error variability.

5. Summary and conclusions

This work quantifies and compares sampling errors in linear estimates of component wind fields derived from various scatterometer datasets.

A simple simulation where NSCAT sampling was applied to ECMWF analyzed surface wind fields demonstrated the magnitude and space–time heterogeneity of the sampling errors that can be expected when constructing maps from a scatterometer dataset. Sampling errors can be a significant fraction of the wind field being mapped. The overall magnitude and variability of the sampling errors change temporally and geographi-
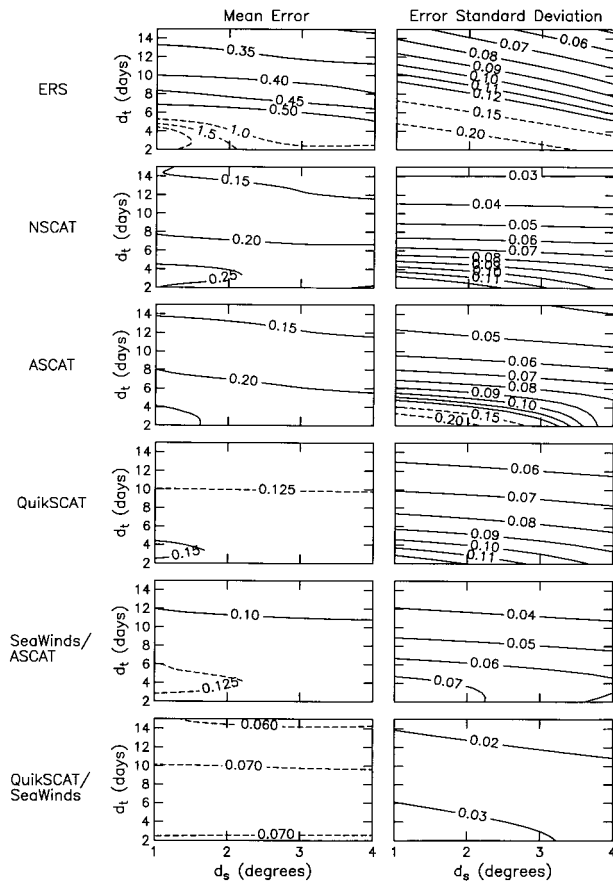
FIG. 16. Mean (left panels) and standard deviation (right panels) of relative sampling errors calculated using ρ_v at 1° intervals between 150° and 170°W and at 1-day intervals over 20 days, at 10°, 25°, 40°, and 50°N, plotted as functions of (isotropic) spatial and temporal loess half-spans. (a) ERS, (b) NSCAT, (c) ASCAT, (d) QuikSCAT, (e) SeaWinds/ASCAT, and (f) QuikSCAT/SeaWinds. Additional dashed-line contours are used when the contour interval is changed for clarity.

cally. Increasing the amount of smoothing applied to the simulated dataset generally reduces both the mean and the variability of the sampling errors, in exchange for the loss of locally high resolution.

With the exception of ERS, all single-scatterometer scenarios examined provide nearly complete spatial sampling within 48 h between the equator and 60°N (Fig. 5). The tandem pairs SeaWinds/ASCAT and QuikSCAT/SeaWinds provide nearly complete spatial data coverage on approximately daily and 12-h intervals, respectively.

The temporal sampling characteristics of all six scatterometer scenarios considered here are complex and geographically variable. The juxtaposition of the measurement swaths results in distinctive burst sampling patterns in time, characterized by sets of closely spaced samples interspersed with longer data gaps (Fig. 6). The duration of the bursts of closely spaced samples and the duration of the gaps that separate them change with both

latitude and longitude, depending on the details of the swath geometry and orbital characteristics of the spacecraft carrying the scatterometer. The mean revisit interval (Fig. 7) provides an aggregate measure of the temporal sampling provided by each scenario. Revisit intervals vary with latitude and generally decrease with increasing latitude. The mean revisit interval is an overly simplistic characterization of scatterometer sampling patterns. The distribution of revisit intervals may be highly skewed and can change radically over scales as short as 1° of latitude (Fig. 8).

Sampling errors are quantified in section 4 based on the expected squared bias (ESB) of loess estimates. Because of the heterogeneous sampling patterns of the scatterometers, ESB calculations on an extensive space–time grid are required to describe the sampling errors. To make this large set of calculations tractable, several modifications to previous ESB calculations were devised that allow more efficient evaluation of the basic integral (6) defining the ESB. The usual implementation of the loess smoother uses the tricubic weighting function. Simplification was achieved by using Gaussian weights instead. The bias of the modified loess estimate was calculated with respect to an ideal loess estimate, rather than to the ideal low-pass filter used in earlier studies. Finally, a functional form for the space–time autocorrelation function was selected that both reduced computational requirements and provided a reasonable model for characterizing the second-order statistics of component wind fields. The end result of these modifications is a closed-form expression that allows extensive application of the ESB as a measure of sampling error.

The ESB calculated here is specific to the loess smoother. Most interpolation algorithms act as low-pass filters. To the extent that the transfer function of another interpolation algorithm can be compared to that of the loess smoother [e.g., by choosing the amount of smoothing applied so that the half power point of the transfer function matches that of (9)], these results are generally applicable, given the autocorrelation functions assumed here. The sampling errors calculated here do not apply to interpolation methods that allow for propagating signals or various physically based assimilation schemes.

Maps of the relative sampling errors of loess estimates at a given time show that the sampling errors vary temporally and geographically in patterns that can be associated with the measurement swaths. Sampling errors shift in time and depend on the amount of smoothing applied. The existence of a general dependence of the mean and variability of the sampling errors on latitude is confirmed when the mean and variability of sampling errors are calculated over time–longitude grids for a range of latitudes. Comparing this result with the revisit interval distributions (Fig. 8) shows that both the mean and variation of the sampling errors are closely linked to the temporal sampling.

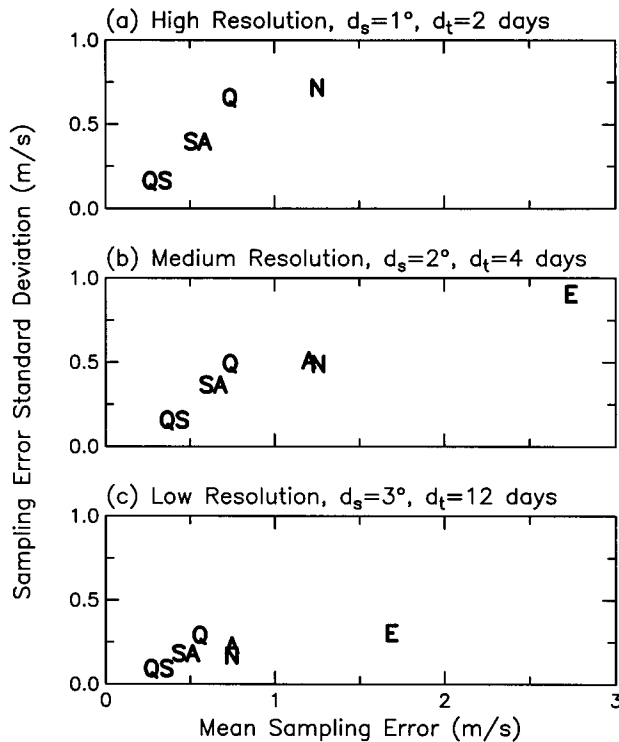The strong dependence of the sampling errors on the

FIG. 17. Standard deviation versus mean of the sampling errors calculated as in Fig. 16, assuming $\sigma_h = 5$ m s^{-1}, for (a) high resolution, $d_s = 1°$, $d_t = 2$ days; (b) medium resolution, $d_s = 2°$, $d_t = 4$ days; and (c) low resolution, $d_s = 3°$, $d_t = 12$ days. E = ERS, N = NSCAT, A = ASCAT, Q = QuikSCAT, SA = SeaWinds/ASCAT, and QS = QuikSCAT/SeaWinds.

details of the temporal sampling was further demonstrated from Fig. 15. For $d_s = 2°$ and $d_t = 4$ days, the sampling error is not particularly sensitive to the spatial scales imposed by the choice of autocorrelation function. There is, however, a small but noticeable reduction of the sampling error when longer timescales are assumed. The dependence of the sampling errors on the degree of smoothing applied is summarized in Fig. 16, which provides guidance for the degree of smoothing to use when constructing large-area maps of component winds.

A summary comparison of the various scatterometer mission scenarios is provided by Fig. 17. For this discussion, we define "high resolution" as retaining space and timescales shorter than 1° and 2 days (i.e., $d_s = 1°$, $d_t = 2$ days); "medium resolution" as retaining space and timescales shorter than 2° and 4 days ($d_s = 2°$, $d_t = 4$ days as in Figs. 12 and 13); and "low resolution" as retaining space scales and timescales shorter than 3° and 12 days ($d_s = 3°$, $d_t = 12$ days as in Fig. 14). The means and standard deviations of the relative sampling errors for each scatterometer mission scenario were taken from Fig. 16 (using ρ_v) and converted to absolute errors by assuming (based on Fig. 11 and the discussion in section 3c) $\sigma_h = 5$ m s^{-1}. (As a test of the sensitivity of these results to the assumed spatial decorrelation

scales, the error means and standard deviations for Fig. 17 were recalculated using ρ_{vs} and ρ_{vl}. For all of the points plotted, only small differences of less than a few tenths of a meter per second occur, and hence the conclusions are unchanged.)

QuikSCAT, SeaWinds/ASCAT, and QuikSCAT/SeaWinds all provide high-resolution maps with sampling errors that are less than 1 m s^{-1} in both mean and standard deviation. Of the three, QuikSCAT/SeaWinds is clearly superior. NSCAT has about the same overall level of error variability as QuikSCAT, but 0.5 m s^{-1} greater mean error. ERS and ASCAT are off the scale of this plot (the mean and standard deviation for ASCAT are 1.5 and 1.7 m s^{-1}, respectively, and those for ERS are extremely large). At the medium resolution level, maps derived from SeaWinds/ASCAT and QuikSCAT/SeaWinds have errors similar in mean and standard deviation to the high-resolution case. Medium-resolution sampling errors for ERS are quite high, nearly 3 m s^{-1}, with a variability of 0.9 m s^{-1}.

With the exception of ERS, all of the scatterometer scenarios can be used to make low-resolution maps with mean errors below the 1 m s^{-1} level with low (less than 0.5 m s^{-1}) error standard deviation. ERS can be used to make low-resolution maps with fairly uniform errors (error standard deviation of about 0.3 m s^{-1}) but higher (1.7 m s^{-1}) mean error.

Figure 17 demonstrates the importance of the broad spatial coverage and corresponding improved temporal sampling provided by the single-swath SeaWinds instrument, as well as the improvement in temporal coverage gained when two SeaWinds-type scatterometers are combined in coordinated orbits. At the other extreme, the poor performance of a single, narrow measurement swath such as ERS is readily apparent.

APPENDIX

ESB Calculations

a. Locally weighted regression smoothers

1) SMOOTHER WEIGHTS FOR THE DISCRETE CASE

Calculation of the ESB requires the smoother weights α_j from Eq. (3). Greenslade et al. (1997) described a "response method" for calculating the weights. Following is a more straightforward analytical method.

Locally weighted regression provides an estimate $\hat{h}(\mathbf{x}_0)$ of $h(\mathbf{x}_0)$ where $\hat{h}(\mathbf{x})$ is a linear combination of M basis functions $q_k(\mathbf{x})$,

$$\hat{h}(\mathbf{x}) = \sum_{k=1}^{M} \gamma_k q_k(\mathbf{x}),$$

with coefficients $\boldsymbol{\gamma}^{\mathrm{T}} = [\gamma_1, \ldots, \gamma_M]$ selected to minimize

$$\Phi(\boldsymbol{\gamma}) = \sum_{j=1}^{M} w(\|\tilde{\mathbf{x}}_j\|)\{\hat{h}(\mathbf{x}_j) - g_j\}^2,$$

where w is a nonnegative, monotonically decreasing weighting function,

$$\tilde{\mathbf{x}}_j = \left(\frac{x_j - x_0}{d_x}, \frac{y_j - y_0}{d_y}, \frac{t_j - t_0}{d_t} \right),$$

and d_x, d_y, and d_t are the *half-spans* of the smoother. Larger half-spans incorporate more data and result in a smoother estimate.

Minimizing Φ with respect to $\boldsymbol{\gamma}$ results in the linear system $\mathbf{X}\boldsymbol{\gamma} = \boldsymbol{\eta}$ where

$$\mathbf{X}_{kl} = \sum_{j=1}^{N} q_k(\mathbf{x}_j)q_l(\mathbf{x}_j)w(\|\tilde{\mathbf{x}}\|), \quad \text{and}$$

$$\boldsymbol{\eta}^{\mathrm{T}} = \left[\sum w(\|\tilde{\mathbf{x}}_j\|)g_j q_1(\mathbf{x}_j), \ldots, \sum w(\|\tilde{\mathbf{x}}_j\|)g_j q_M(\mathbf{x}_j) \right].$$

For locally weighted quadratic regression in three dimensions, $M = 10$, and

$$q_1 = 1, \qquad q_2 = x, \qquad q_3 = x^2, \qquad q_4 = y,$$

$$q_5 = y^2, \qquad q_6 = xy, \qquad q_7 = t, \qquad q_8 = t^2,$$

$$q_9 = xt, \qquad q_{10} = yt. \tag{A1}$$

Assuming without loss of generality that $\mathbf{x}_0 = 0$, it follows that $\hat{h}(0) = \gamma_1$. Now,

$$\gamma_1 = \sum_{k=1}^{M} \mathbf{X}_{1k}^{-1}\eta_k,$$

so, writing $\chi_k = \mathbf{X}_{1k}^{-1}$, $w_j = w(\|\tilde{\mathbf{x}}_j\|)$ and $q_{jk} = q_k(\mathbf{x}_j)$,

$$\gamma_1 = \sum_{j=1}^{N} \left\{ w_j \sum_{k=1}^{M} \chi_k g_{jk} \right\} g_j.$$

This has the form of a linear estimator $\hat{h} = \Sigma \, \alpha_j g_j$, with smoother weights

$$\alpha_j = w_j \sum_{k=1}^{M} \chi_k q_j. \tag{A2}$$

2) CONTINUOUS CASE

We seek to compare the estimate given by (3) and (A2) with the "ideal" case, $\bar{h}$, defined to be the loess estimate obtained from a continuous sampling of the function h. Using the same M basis functions q_k defined in (A1), and again assuming that $\mathbf{x}_0 = 0$, and $\tilde{\mathbf{x}} = (x/d_x, y/d_y, t/d_t)$, we seek the minimum of

$$\Phi(\boldsymbol{\gamma}) = \int_{-\infty}^{\infty} w(\|\tilde{\mathbf{x}}\|)\{\hat{h}(\mathbf{x}) - h(\mathbf{x})\}^2 \, d\mathbf{x},$$

yielding a set of linear constraints $\mathbf{X}\boldsymbol{\gamma} = \boldsymbol{\eta}$ where

$$\mathbf{X}_{kl} = \int_{-\infty}^{\infty} w(\|\tilde{\mathbf{x}}\|)q_k(\mathbf{x})q_l(\mathbf{x}) \, d\mathbf{x} \quad \text{and}$$

$$\eta_k = \int_{-\infty}^{\infty} w(\|\tilde{\mathbf{x}}\|)q_k(\mathbf{x})h(\mathbf{x}) \, d\mathbf{x}. \tag{A3}$$

Defining χ_k as before,

$$\bar{h} = \int_{-\infty}^{\infty} \left\{ w(\|\tilde{\mathbf{x}}\|) \sum_{k=1}^{M} \chi_k q_k(\mathbf{x}) \right\} h(\mathbf{x}) \, d\mathbf{x}.$$

Thus, h is a linear functional of h,

$$\bar{h} = \int_{-\infty}^{\infty} \alpha(\mathbf{x})h(\mathbf{x}) \, d\mathbf{x} = \int_{-\infty}^{\infty} P_\alpha^*(\mathbf{s})H(\mathbf{s}) \, d\mathbf{s},$$

where

$$\alpha(\mathbf{x}) = w(\|\tilde{\mathbf{x}}\|) \sum_{k=1}^{M} \chi_k q_k(\mathbf{x}), \tag{A4}$$

is the continuous weighting function (analogous to the smoother weights α_j) and P_α is the Fourier transform of α.

The coefficients χ_k depend on the matrix $\mathbf{X}$ defined by (A3). Since $w(\|\tilde{\mathbf{x}}\|)$ is an even function of all three variables, only those products of basis functions $q_k(\mathbf{x})q_l(\mathbf{x})$ that are even functions of x, y and t result in nonzero integrals in (A3). For the basis under consideration, there are 10,

$$X_0 = \int w(\|\mathbf{x}\|) \, d\mathbf{x}, \qquad X_{x^2} = \int x^2 w(\|\tilde{\mathbf{x}}\|) \, d\mathbf{x},$$

$$X_{y^2} = \int y^2 w(\|\mathbf{x}\|) \, d\mathbf{x}, \qquad X_{t^2} = \int t^2 w(\|\tilde{\mathbf{x}}\|) \, d\mathbf{x},$$

$$X_{x^4} = \int x^4 w(\|\mathbf{x}\|) \, d\mathbf{x}, \qquad X_{y^4} = \int y^4 w(\|\tilde{\mathbf{x}}\|) \, d\mathbf{x},$$

$$X_{t^4} = \int t^4 w(\|\mathbf{x}\|) \, d\mathbf{x}, \qquad X_{x^2y^2} = \int x^2 y^2 w(\|\tilde{\mathbf{x}}\|) \, d\mathbf{x},$$

$$X_{x^2 t^2} = \int x^2 t^2 w(\|\mathbf{x}\|) \, d\mathbf{x}, \qquad X_{t^2 t^2} = \int y^2 t^2 w(\|\tilde{\mathbf{x}}\|) \, d\mathbf{x},$$

comprising a sparse matrix that is easily inverted to yield the χ_k.

3) THE GAUSSIAN WEIGHTING

In its usual form, the local weighted regression smoother uses the tricubic weighting function:

$$w_t(\|\tilde{\mathbf{x}}\|) = \begin{cases} (1 - \|\tilde{\mathbf{x}}\|^3)^3, & \text{if } \|\tilde{\mathbf{x}}\| \leq 1 \\ 0, & \text{otherwise.} \end{cases}$$

While this function has a number of properties that make it an appropriate choice for a local regression smoother (Cleveland 1979), it complicates both analytical and numerical calculations. Another choice is the Gaussian weighting function

$$w_G(\|\tilde{\mathbf{x}}\|) = e^{-\sigma\|\tilde{\mathbf{x}}\|^2}, \tag{A5}$$

where σ is a parameter to be determined. With this choice, much simplification is obtained. The continuous weights in (A4) are defined by the separable function

$$\alpha_G(\|\tilde{\mathbf{x}}\|) = \pi^{1/3} \frac{e^{-\sigma\|\tilde{\mathbf{x}}\|^2}}{d_x d_y d_t \sigma^{1/3}} \left\{ \frac{5}{2} - \sigma\|\tilde{\mathbf{x}}\|^2 \right\}, \tag{A6}$$

with a separable Fourier transform P_G given by equation (9) in section 3.

4) CALIBRATING THE GAUSSIAN SMOOTHER

The free parameter σ in (A5) allows calibration of the Gaussian-weighted smoother. Consider the ideal low-pass filter P_I [Eq. (7)] with unit wavenumber–frequency cutoffs and the transfer function P_G with unit half-spans. Then the value of σ that minimizes

$$\Phi(\sigma) = \int_{-\infty}^{\infty} \|P_I(\mathbf{s}) - P_G(\mathbf{s})\|^2 \, d\mathbf{s}, \tag{A7}$$

provides a smoother that is closest in mean square to an ideal low-pass filter with $(d_x, d_y, d_t) = (1/k_c, 1/l_c, 1/f_c)$. Direct minimization of (A6) yields $\sigma = 4.70$.

b. Efficient ESB calculations

Using the notation presented in section 3, and P_G, the transfer function for the ideal, Gaussian-weighted loess smoother [Eq. (9)], Eq. (6) may be rewritten as

$$E[(\bar{h} - E[\hat{h}])^2]/\sigma_h^2$$

$$= \sum_{jk} \alpha_j \alpha_k \rho(\|\mathbf{x}_j - \mathbf{x}_k\|)$$

$$- 2 \sum_j \alpha_j \int_{-\infty}^{\infty} e^{i2\pi(kx_j+ly_j-ft_j)} P_G^*(\mathbf{s}) S(\mathbf{s}) \, d\mathbf{s}$$

$$+ \int_{-\infty}^{\infty} \int_{-\infty}^{\infty} \|P_G(\mathbf{s})\|^2 S(\mathbf{s}) \, d\mathbf{s}. \tag{A8}$$

Here, S is the normalized power spectral density of h and the Fourier transform of the autocorrelation function ρ,

$$S(\mathbf{s}) = \pi^{1/3} s_x s_y s_t e^{-\pi^2\|\tilde{\mathbf{s}}\|^2}$$

$$\times \left\{ K + \pi^2 \left[\left(\frac{s_x^2 k}{L_x}\right)^2 + \left(\frac{s_y^2 l}{L_y}\right)^2 + \left(\frac{s_t^2 f}{L_t}\right)^2 \right] \right\}, \tag{A9}$$
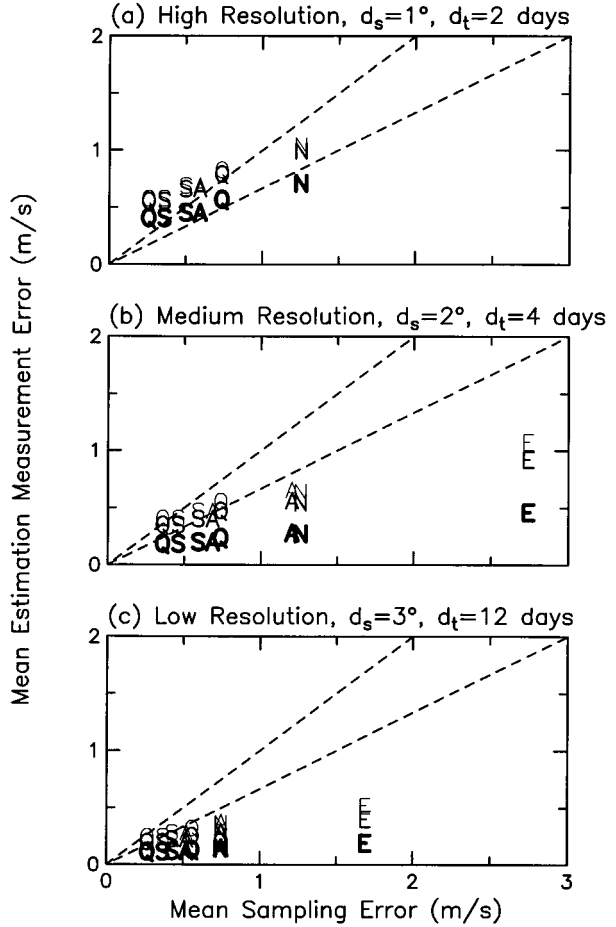
where $\tilde{\mathbf{s}} = (s_x k, s_y l, s_t f)$, and

FIG. A1. Mean estimation measurement error versus mean sampling error (a) high resolution, $d_s = 1°$, $d_t = 2$ days; (b) medium resolution, $d_s = 2°$, $d_t = 4$ days; and (c) low resolution, $d_s = 3°$, $d_t = 12$ days. E = ERS, N = NSCAT, A = ASCAT, Q = QuikSCAT, SA = SeaWinds/ASCAT, and QS = QuikSCAT/SeaWinds. Measurement errors calculated assuming independent errors are heavy type, those based on the 100-km and 200-km decorrelation scales are shown as medium and thin types, respectively. The dashed lines have slopes of 1 and 1/2.

$$K = 1 - \frac{1}{2}\left[\left(\frac{s_x}{L_x}\right)^2 + \left(\frac{s_y}{L_y}\right)^2 + \left(\frac{s_t}{L_t}\right)^2 \right].$$

A necessary and sufficient condition for ρ to be positive definite is that K be greater than 0, which obtains for all of the examples used in this paper.

Both P_G and S can be written as the sums of products of even functions of k, l, and f, so that the integrals in the second and third terms of (A8) are the sums of products of one-dimensional integrals with the form

$$\int_0^{\infty} x^{2n} e^{-\beta x^2} \cos(ax) \, dx$$

$$= (-1)^n \frac{\sqrt{\pi}}{(2\beta)^{2n+1}} \exp\left(-\frac{a^2}{4\beta^2}\right) H_{2n}\left(\frac{a}{2\beta}\right),$$

where $H_n(x)$ are the Hermite polynomials (Gradshteyn and Ryzhik 1980). Given this analytical form of the integrals in (A8), the largest computational burden lies in the quadratic form constituting the first term of that equation; the error estimates usually obtained from objective estimation schemes share this property.

c. Variance of the estimates

The calculations discussed in section 4 considered only the effects of sampling errors. It is of interest to assess the importance of measurement error contributions [Eq. (11)] to the total mean squared error [Eq. (1)]. Variances of the loess estimates studied here were calculated as described in section 3d. For comparison with the summary results for sampling errors shown in Fig. 17, Eq(11) was evaluated for loess estimates with smoothing parameters d_s and d_t corresponding to the high-, medium-, and low-resolution cases, on the same space–time grid used to generate Fig. 17. The square root of the variance was averaged over the grid to produce ''mean estimation measurement errors.'' Figure A1 shows a comparison of mean sampling errors with the mean estimation measurement errors derived from the three characterizations of the measurement errors, for the three resolution levels.

Mean estimation measurement and sampling errors become comparable in the high-resolution case, for which the mean estimation measurement errors calculated assuming correlated errors are more than one-half the magnitude of the mean sampling errors; for QuikSCAT and the tandem missions, the mean estimation measurement errors slightly exceed the mean sampling errors (as in Fig. 17a, ERS and ASCAT are not plotted in this figure). For the medium-resolution case, the mean estimation measurement errors are greater than one-half of the mean sampling errors for correlated measurement errors for QuikSCAT, SeaWinds/ASCAT, and QuikSCAT/SeaWinds. For the low-resolution case, the mean estimation measurement errors are all less than one-half of the mean sampling errors. Except for the high-resolution case, it seems reasonable to conclude that sampling error is generally the dominant

component of the total mean-squared error in maps of scatterometer data.

REFERENCES

Chelton, D. B., and M. G. Schlax, 1994: The resolution capability of an irregularly sampled dataset: With application to Geosat altimeter data. *J. Atmos. Oceanic Technol.,* **11,** 534–550.

Cleveland, W. S., 1979: Robust locally weighted regression and smoothing scatterplots. *J. Amer. Stat. Assoc.,* **74,** 829–836.

——, and S. J. Devlin, 1988: Locally weighted regression: An approach to regression analysis by local fitting. *J. Amer. Stat. Assoc.,* **83,** 596–610.

Freilich, M. H., and D. B. Chelton, 1986: Wavenumber spectra of Pacific winds measured by the Seasat scatterometer. *J. Phys. Oceanogr.,* **16,** 741–757.

——, and R. S. Dunbar, 1999: The accuracy of the NSCAT-1 vector winds: Comparisons with National Data Buoy Center buoys. *J. Geophys. Res.,* **104,** 11 231–11 246.

Gradshteyn, I. S., and I. M. Ryzhik, 1980: *Table of Integrals, Series, and Products.* Academic Press, 1160 pp.

Greenslade, D. J. M., D. B. Chelton, and M. G. Schlax, 1997: The midlatitude resolution capability of sea level fields constructed from single and multiple satellite altimeter datasets. *J. Atmos. Oceanic Technol.,* **14,** 849–870.

Journel, A. G., and C. J. Huijbregts, 1978: *Mining Geostatistics.* Academic Press, 600 pp.

Kelly, K. A., and M. J. Caruso, 1990: A modified objective mapping technique for scatterometer wind data. *J. Geophys. Res.,* **95,** 13 483–13 496.

Legler, D. M., and J. J. O'Brien, 1985: Development and testing of a simple assimilation technique to derive average wind fields from simulated scatterometer data. *Mon. Wea. Rev.,* **113,** 1791–1800.

Liu, W. T., W. Tang, and P. S. Polito, 1998: NASA scatterometer provides global ocean-surface wind fields with more structures than numerical weather prediction. *Geophys. Res. Lett.,* **25,** 761–764.

Naderi, F. M., M. H. Freilich, and D. G. Long, 1991: Spaceborne radar measurement of wind velocity over the ocean—An overview of the NSCAT scatterometer system. *Proc. IEEE,* **97,** 850–866.

Press, W. H., S. A. Teukolsky, W. T. Vettering, and B. P. Flannery, 1992: *Numerical Recipes in FORTRAN.* Cambridge University Press, 963 pp.

Schlax, M. G., and D. B. Chelton, 1992: Frequency domain diagnostics for linear smoothers. *J. Amer. Stat. Assoc.,* **87,** 1070–1081.

Zeng, L., and G. Levy, 1995: Space and time aliasing structure in monthly mean polar-orbiting satellite data. *J. Geophys. Res.,* **100,** 5133–5142.